Comparison of scanning aerosol LIDAR and *in-situ* measurements of aerosol physical properties and boundary layer heights

Hengheng Zhang[1], Christian Rolf[2], Ralf Tillmann[3], Christian Wesolek[3], Frank Gunther Wienhold[4], Thomas Leisner[1], and Harald Saathoff[1]

[1]Institute of Meteorology and Climate Research, Karlsruhe Institute of Technology, Eggenstein-Leopoldshafen, Karlsruhe, Germany
[2]Institute of Energy and Climate Research - Stratosphere (IEK-7), Reseach Center Jülich, Wilhelm-Johnen-Straße, Jülich, Germany
[3]Institute of Energy and Climate Research - Troposphere (IEK-8), Reseach Center Jülich, Wilhelm-Johnen-Straße, Jülich, Germany
[4]Institute for Atmospheric and Climate Science, ETH Zürich, Universitätstrasse 16, Zürich, Switzerland

Correspondence: Hengheng Zhang (hengheng.zhang@kit.edu) and Harald Saathoff (Harald.Saathoff@kit.edu)

Abstract. The spatial-temporal distribution of aerosol particles in the atmosphere has a great impact on radiative transfer, clouds, and air quality. Modern remote sensing methods as well as airborne *in-situ* measurements by unmanned aerial vehicles (UAV) or balloons are suitable tools to improve our understanding of the role of aerosol particles in the atmosphere. To validate the measurement capabilities of three relatively new measurement systems and to bridge the gaps that are often encountered between remote sensing and *in-situ* observation as well as to investigate aerosol particles in and above the boundary layer, we conducted two measurement campaigns and collected a comprehensive dataset employing a scanning aerosol LIDAR, a balloon-borne radiosonde with the Compact Optical Backscatter Aerosol Detector (COBALD), an optical particle counter (OPC) on ~~a~~ an UAV, as well as a comprehensive set of ground-based instruments. The extinction coefficients calculated from near-ground-level aerosol size distributions measured *in-situ* are well correlated with those retrieved from LIDAR measurements with a slope of 1.037 ± 0.015 and a Pearson correlation coefficient of 0.878, respectively. Vertical profiles measured by an OPC-N3 on ~~a~~ an UAV show similar vertical particle distributions and boundary layer heights as LIDAR measurements. However, the sensor, OPC-N3, shows a larger variability in aerosol ~~backscatter~~ backscattering coefficient measurements with a Pearson correlation coefficient of only 0.241. In contrast, the COBALD data from a balloon flight are well correlated with LIDAR-derived backscatter data from the near ground level up to the stratosphere with a slope of 1.063 ± 0.016 and a Pearson correlation coefficient of 0.925, respectively. This consistency between LIDAR and COBALD data reflects a good data quality of both methods and proves that LIDAR can provide reliable and spatial distributions of aerosol particles with high spatial and temporal resolutions. This study shows that the scanning LIDAR has the capability to retrieve ~~backscatter~~ backscattering coefficients near ground level (from 25 m to 50 m above ground level) when it conducts horizontal measurement which isn't possible for vertically pointing LIDAR. These near-ground-level retrievals compare well with ground-level *in-situ* measurements. In addition, *in-situ* measurements on the balloon and UAV validated scanning LIDAR retrievals within and above the boundary layer. The scanning aerosol LIDAR allows us to measure aerosol particle distributions and profiles from the ground level to the stratosphere with an accuracy equal or better than *in-situ* measurements and with a similar spatial resolution.

1 Introduction

The large varieties of aerosol spatial-temporal distributions in the atmosphere cause large uncertainties in radiative forcing
25 globally (Ramanathan et al., 2001) and these uncertainties have a great impact on climate change simulations (Stocker, 2014).
The distributions and evolution of aerosol are related to the emission of aerosols (Grythe et al., 2014; Tegen and Schepanski,
2018; Hamilton et al., 2022) and ~~the~~ their loss pathway (Poreh and Cermak, 1964; Cheng et al., 2011; Xiang et al., 2019; Xue
et al., 2022). In addition, another important factor affecting radiative forcing is aerosol optical properties (e.g. single ~~scatter~~
scattering albedo (SSA), LIDAR ratio, ~~scatter~~ scattering and absorption coefficients) (Alam et al., 2011; Romshoo et al., 2021),
30 which also have large varieties for different types of aerosols (Lesins et al., 2002; Floutsi et al., 2022).
Many methods have been used to measure the spatial-temporal distribution ~~and~~ of aerosol optical parameters regionally and
globally. One of the most successful instruments for this purpose is the Moderate Resolution Imaging Spectroradiometer
(MODIS) on Terra and Aqua satellites (Filonchyk and Hurynovich, 2020; Qin et al., 2021). MODIS can provide column-
integrated optical parameters like aerosol optical depth (AOD), Ångström exponent (AE), and single ~~scatter~~ scattering albedo
35 (SSA) to study the optical properties of mineral dust (Kaufman et al., 2005; Ginoux et al., 2012), urban aerosol (More et al.,
2013; Munchak et al., 2013), forest fire smoke (MAE, 2009; Huesca et al., 2009) etc. Another successful satellite mission is the
Cloud-Aerosol ~~LIDAR~~ Lidar and Infrared Pathfinder Satellite Observations (CALIPSO). CALIPSO combines an active LIDAR
instrument with passive infrared and visible ~~imagers~~ images to probe the vertical structure and properties of thin clouds and
aerosols over the globe ~~(Winker et al., 2009; Wang et al., 2021; Salehi et al., 2021).~~ (Winker et al., 2009; Wang et al., 2021; Salehi et al., 20
40 . China launched its first space-borne aerosol-cloud high-spectral-resolution lidar (ACHSRL) on April 16, 2022, which is
capable for high accuracy profiling of aerosols and clouds around the globe (Ke et al., 2022). Also, the Earth Cloud, Aerosol
and Radiation Explorer (EarthCARE) is a satellite mission implemented by the European Space Agency (ESA), in cooperation
with the Japan Aerospace Exploration Agency (JAXA), to measure global profiles of aerosols, clouds and precipitation
properties together with radiative fluxes and derived heating rates, due for launch in May 2024 (Wehr et al., 2023).
45 In addition to these satellite missions, ground-based remote sensing methods are used to investigate aerosol optical proper-
ties ~~(Kotthaus et al., 2023)~~ (Adam et al., 2020; Mylonaki et al., 2021). Over the last decades, many ground-based observation
networks were established to investigate aerosol properties regionally and globally. For example, the AERONET (AErosol
RObotic NETwork) project is a federation of ground-based remote sensing aerosol networks that provides globally distributed
observations of spectral aerosol optical depth (AOD), inversion products, and precipitation water in diverse aerosol regimes
50 (Holben et al., 1998; Prasad and Singh, 2007; Mielonen et al., 2009). The Micro-Pulse LIDAR Network (MPLNET) is a fed-
erated network of Micro-Pulse LIDAR (MPL) systems designed to measure aerosol and cloud vertical structure, and boundary
layer heights (Welton et al., 2006; Lolli et al., 2018). The European Aerosol Research ~~LIDAR~~ Lidar Network (EARLINET) is
a multi-wavelength LIDAR network designed to create a quantitative, comprehensive, and statistically significant database for
the horizontal, vertical, and temporal distribution of aerosols on a continental scale (Pappalardo et al., 2014a; Marinou et al.,
55 2017).
Aerosol elastic scattering lidar is widely used in lidar observation networks as it can provide detailed information with

high spatial and temporal resolution. However, retrieving backscattering coefficients from this kind of lidar data requires assumptions of lidar ratios and reference values (Fernald, 1984b; Klett, 1985b). One of the successfully used technology to overcome this problem is the Raman lidar (Wandinger, 2005; Groß et al., 2015; Baars et al., 2016; Hu et al., 2022). Another

60   widely used technology is the high spectral resolution lidar (HSRL) (Liu et al., 1999) which used narrow-band filter (e.g. atom or molecule filter) to separate signals from molecule and particle backscatter (Piironen and Eloranta, 1994). And this HSRL allows us better to investigate aerosol optical properties (Burton et al., 2012, 2014; Groß et al., 2013). Recently, a HSRL that uses an interferometer as filter has been deployed at other wavelengths. The recently launched Doppler Wind Lidar, ALADIN, uses this technology to measure tropospheric wind profiles on a global scale but can also obtain vertical aerosol profiles

65   (Schillinger et al., 2003).

In-situ measurements can also help us better understand aerosol optical properties. The most common instruments are the nephelometer and aethalometer, which can measure the wavelength-dependent optical parameters like ~~scatter~~ scattering and absorption coefficients of aerosol particles ~~(Anderson et al., 1996; Drinovec et al., 2015)~~(Anderson et al., 1996; Zieger et al., 2011; Drinovec et al., 2015). The aerosol optical parameters are determined by particle size distribution, particle shape, and complex refractive index

70   (Bohren and Huffman, 2008; Yao et al., 2022). The size distribution can be measured by different kinds of particle sizers like Scanning Mobility Particle Sizer (SMPS), Optical Particle Counter (OPC), and Aerodynamic Particle Sizer (APS). The aerosol complex refractive index is related to the aerosol chemical composition which can be measured by aerosol mass spectrometry as well as the relative humidity (Zieger et al., 2015). For decades, these *in-situ* aerosol characterization instruments not only provided valuable datasets at ground level (Huang et al., 2019; Jiang et al., 2022) but also were deployed on aircraft, balloons,

75   mountains (Zieger et al., 2012), and unmanned aerial vehicles to get vertical profiles of aerosol parameters (Bahreini et al., 2003; Zhen et al., 2018; Brunamonti et al., 2021).

~~LIDAR is a powerful tool to measure the spatial distribution and optical parameters of aerosol (Böckmann et al., 2004; Matthais et al., 2004)~~ ~~.~~ Although many results have reported aerosol measurements by LIDAR ~~(Matthias and Bösenberg, 2002; Pappalardo et al., 2014b; Hofer et al., 2020)~~ (Matthias and Bösenberg, 2002; Pappalardo et al., 2014b; Hofer et al., 2020), there are fewer reports on comparison of *in-situ*

80   measurement with LIDAR measurement to quantify uncertainties of LIDAR retrievals ~~(Düsing et al., 2018; Xiafukaiti et al., 2020; Düsing et al., 2018)~~ (Xiafukaiti et al., 2020; Düsing et al., 2018). In addition, most vertical pointing LIDAR systems have overlap gap between the detector's field of view and the laser beam from tens to around one thousand meters, which makes it difficult to get valid measurement near the surface (Wandinger and Ansmann, 2002) to compare with ground level *in-situ* measurements. However, scanning LIDAR can conduct horizontal measurements allowing to get vertical profiles of aerosol particles and boundary layer

85   structure near the ground level (Althausen et al., 2000). In addition, scanning aerosol LIDAR can also determine LIDAR ratios to reduce the uncertainties in the LIDAR retrievals (Fernald, 1984a; Zhang et al., 2022).

In recent years, vertical profiles of aerosol are also investigated more and more by Unmanned Aerial Vehicles (UAV) and LIDAR. For example, Liu et al. (2020) used the UAVs and LIDAR to study the vertical distribution of $PM_{2.5}$ and interactions with the atmospheric boundary layer during the development of heavy haze pollution. Ferrero et al. (2019) compared the

90   ~~backscatter~~ backscattering coefficient retrieved from LIDAR with that calculated from aerosol size distributions measured by OPC on tethered balloons in the Arctic to study the role of aerosol chemistry and dust composition in a closure experiment.

Zhang et al. (2021) compared boundary layer heights retrieved from aerosol LIDAR and tethered balloon measurements in semi-arid regions. Liu et al. (2021) found that wind shear generating turbulence reshaped the vertical profiles of parameters such as potential temperature (θ) and $PM_{2.5}$ in the nocturnal boundary layer, which was the key factor leading to the de-
95 velopment of entrainment at nighttime. Reineman et al. (2016) used ship-launched fixed-Wing UAVs to measure the marine atmospheric boundary layer and ocean surface processes. In addition, the vertical profiles of atmospheric parameters related to aerosol process such as temperature (Zarco-Tejada et al., 2012), relative humidity (Spiess et al., 2007), wind (Spiess et al., 2007) and ozone concentration (Guimarães et al., 2019) are also obtained from UAV flights.

However, to our best knowledge, so far no dedicated comparison of scanning LIDAR measurement with *in-situ* observation
100 has been performed over a wide altitude range ~~. Therefore~~and over such a long time period for comparison at ground level (e.g. one month dataset with 10 minute resolution). Also in order to bridge the gaps that are often encountered between remote sensing and *in-situ* observation, we compared datasets on aerosol spatial-temporal distributions and ~~evolutions~~ evolution combining remote sensing and *in-situ* measurements. Two field campaigns were conducted employing a scanning aerosol LIDAR, a radiosonde with a backscatter sensor, an OPC on a UAV, and a comprehensive set of ground-level instruments. The first
105 field campaign was conducted in downtown Stuttgart to compare LIDAR retrievals with ground level *in-situ* measurements. The second field campaign was done at the Jülich research center to compare LIDAR retrievals with OPC measurements on a UAV and a COBALD backscatter sensor on a radiosonde. The aim of this work is to compare the different methods in aerosol measurements, to validate scanning LIDAR retrievals, to discuss the uncertainties of the different methods and the boundary layer evolutions from LIDAR and UAV retrievals.

2 Methods

110

Two field campaigns were conducted in downtown Stuttgart and at Jülich research center to compare scanning aerosol LIDAR measurements with different *in-situ* measurements. The first field campaign was conducted from February 5th to March 5th, 2018 in downtown Stuttgart (9.2024° E 48.7986° N, 247 m above sea level) employing a mobile container and a scanning aerosol LIDAR on the roof of the container. The ground-level *in-situ* measurements deployed in this mobile container provided
115 aerosol particle size distributions, aerosol chemical composition, and meteorological information (Huang et al., 2019). The second field campaign was conducted from July 5th to 12th, 2018 at Jülich research center (6.4131° E, 50.9084° N, 110 m above sea level) employing a scanning aerosol LIDAR, a COBALD sensor hosted by a Vaisala RS41-SGP radiosonde, and an OPC on UAV. The scanning LIDAR called KASCAL used in these two field campaigns was developed by Raymetrics (LR111-ESS-D200, Raymetrics Inc.). A UAV (eBee, senseFly) carrying one OPC (OPC-N3, Alphasense Inc.), weather sensors
120 and Global Positioning System (GPS) sensors provided altitude-dependent particle size distribution and also meteorological information above the Jülich research center. In addition, atmospheric parameters like pressure, temperature, relative humidity and wind information from the ground to 30 km above Jülich research center were gathered by a GPS-equipped radiosonde onboard a balloon that carried COBALD to measure altitude-dependent *in-situ* ~~backscatter~~ backscattering coefficients at two wavelengths (455 nm & 940 nm) (Brunamonti et al., 2021). The measurements during this work indicated that the basckatter

was dominated by smaller particles with low depolarisation ratios so that it seemed justified to use a spherical model to represent these aerosol particles (Khlebtsov et al., 2005; Moroz, 2009; Wang et al., 2023). Hence, a Mie code (Leinonen, 2016) was used to calculate extinction coefficients and ~~backseatter~~ backscattering coefficients from aerosol size distributions for comparison with the LIDAR retrieval.

2.1 Scanning aerosol LIDAR

The 3D scanning LIDAR (KASCAL) used in the above two field campaigns has an emission wavelength of 355 nm and is equipped with elastic, depolarization, and vibrational Raman channels, hence allowing to retrieve extinction coefficients, ~~backseatter~~ backscattering coefficients, and depolarization ratios. The laser pulse energy and repetition frequency are 32.1 mJ and 20 Hz, respectively. The laser head, 200 mm telescope, and LIDAR signal detection units are mounted on a rotating platform allowing zenith angles from -7° to 90° and azimuth angles from 0° to 360°. This LIDAR works automatically, time-controlled, and continuously via software developed by Raymetrics. Detailed information can be found at https://www.raymetrics.com/product/3d-scanning-LIDAR, last access: 8 March 2021 (Avdikos, 2015; Zhang et al., 2022). During the first field campaign in downtown Stuttgart, the LIDAR conducted zenith scanns with an elevation angle from 90 ° to 5° in steps of 5°. The measurements at 5° were used over a range representative of an altitude of 25-50 m to compare with ground-level *in-situ* measurements (3.7 m above ground level). It is assumed that these values are comparable within the mixing layer. During the second field campaign at Jülich research center, the LIDAR conducted zenith scans during UAV launch and the measurements at all elevation angles were used to get vertical profiles of aerosols from ground level up to the free troposphere to compare with an OPC measurement on the UAV. In addition, the LIDAR also conducted vertical pointing measurements in the night of July 12th, 2018 at Jülich research center to compare the vertical profiles of ~~backseatter~~ backscattering coefficients from LIDAR retrievals and COBALD measurement on board of a radiosonde.

For the data analysis and calibration of the LIDAR system, we followed the quality standards of the ~~European Aerosol Research LIDAR Network (EARLINET)~~ EARLINET (Freudenthaler, 2016). For data analysis of zenith scans, we ~~determine the vertical backseatter~~ determined the vertical backscattering coefficient profiles using the Klett-Fernald method (Fernald, 1984a; Klett, 1985a). And these vertical profiles of aerosol ~~backseatter~~ backscattering coefficients was used as the reference values for other observation angles. In addition, the measured temperatures and pressures from UAVs and balloons were used to calculate the molecular ~~backseatter~~ backscattering coefficients which can be used in LIDAR retrievals.

The atmospheric boundary layer height can be determined from LIDAR by using the Haar wavelet transform (HWT) method ~~is defined as~~

$$z_{HWT} = \max[w_f(a,b)] = \max \frac{1}{a} \int\limits_{z_{min}}^{z^{max}} X(z) H(\frac{z-b}{a}) \, dz$$

In which w_f is the covariance transform value, $X(z)$ is the range corrected LIDAR signal defined as $X(z) = P(z) * z^2$, and $H(\frac{z-b}{a})$ is the Harr wavelet function as defined as followed:

$$H(\frac{z-b}{a}) = \begin{cases} 1 & b - \frac{a}{2} \leq z \leq b \\ -1 & b \leq z \leq b + \frac{a}{2} \\ 0 & \text{elsewhere} \end{cases}$$

The dilation a was tested and set to be 75 m for this work. Z_{min} and z_{max} are the lower and upper heights for the LIDAR signal profile, respectively. In addition, (Baars et al., 2008). Furthermore, the boundary layer height was also retrieved from vertical profile profiles of potential temperature by using gradient method. (Seidel et al., 2010; Li et al., 2021). the gradient method (Seidel et al., 2010; Li et al., 2021).

2.2 Ground-level *in-situ* measurements in downtown Stuttgart

The ground-level *in-situ* instruments were deployed in a mobile container that was deployed in a parks downtown Stuttgart. Ambient temperature, relative humidity, wind direction, wind speed, global radiation, pressure, and precipitation data were measured by a meteorological sensor (WS700, Lufft GmbH). Trace gases (O_3, CO_2, NO_2, SO_2) were measured with the gas monitors (Environment S.A). Particle number concentrations were recorded with two CPCs (CPC 3774, 3022, TSI Inc,). Particle size distributions were measured with SMPS (DMA: TSI 3080, TSI Inc; CPC: CPC3022, TSI Inc), and OPC (Fidas200, Palas, Inc). The OPC (Fidas200, Palas, Inc.) continuously measured particles in the size range of 0.18 - 18 μm. The OPC used Lorenz-Mie theory to determine the particle number size distribution and this size distribution can be used to calculate extinction coefficients via a Mie code (Leinonen, 2016). In this experiment, Fidas200 was operated with a flow rate of 5 L/min and with a time resolution of 1 s.

Figure 1 shows the workflow in deriving the aerosol extinction coefficients from Mie calculations based on *in-situ* aerosol characterisation instruments. The aerosol sizer (e.g. OPC) can provide dry aerosol particle size distribution, which can be converted to the ambient aerosol size distributions by using hygroscopic growth factors (κ) calculated from aerosol chemical composition using the ISORROPIA II thermodynamic equilibrium model (Fountoukis and Nenes, 2007). The aerosol chemical composition was measured by HR-TOF-AMS (Aerodyne Inc.). Most As most aerosol particles are constrained and well-mixed within the boundary layerand, the aerosol complex refractive index remains almost constant (Raut and Chazette, 2008). Although, the sun photometer is integrating over the whole vertical column, the relatively high aerosol concentrations in the boundary layer dominate (Li et al., 2017). Therefore, it seem justified to use the aerosol complex refractive index derived from a nearby sun photometer (CE-318). Hence, we used the aerosol complex refractive index derived from a nearby sun photometer (CE-318). With ambient aerosol size distribution and complex refractive index, optical parameters (e.g. extinction coefficients) were calculated to compare with LIDAR retrievals. Process flow in deriving aerosol extinction coefficients from Mie calculation and parameters used in Mie calculations. κ_{aero} is the composition dependent hygroscopicity growth factor.
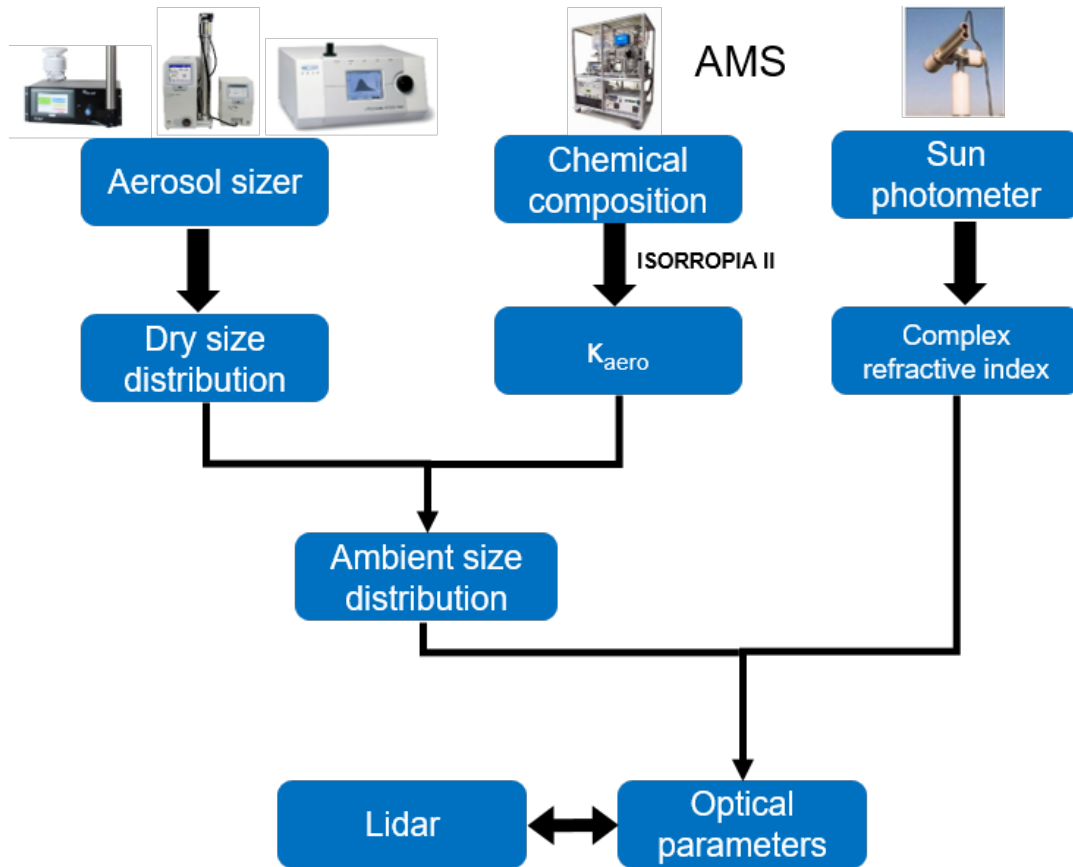
Figure 1. Process flow in deriving aerosol extinction coefficients from Mie calculation and parameters used in Mie calculations. κ_{aero} is the composition dependent hygroscopicity growth factor.

2.3 UAV and balloon-borne measurements at Research Center Jülich

185   Data of an OPC (OPC-N3, Alphasense, Inc) on a UAV and a COBALD backscatter sensor (Institute for Atmospheric and Climate Science, ETH Zurich) on a balloon were collected at Jülich research center in July 2018. The UAV used in this field campaign is a fixed-wing drone (eBee, senseFly) which is operated by the Institute of Energy and Climate Research - Troposphere (IEK-8). Its payload is 320 g at a total weight of 750 g with the highest observation altitude of approximately 1200 m above ground level. The ascent and descent velocity of this UAV was around 3.2 m/s. The measurement sensors were mounted

190   inside the UAV. The size distributions were measured in real-time with a time resolution of 1.6 s by OPC-N3. Additionally, atmospheric parameters such as air temperature, air pressure, relative humidity, wind speed, and wind direction were measured with a temporal resolution of 1 s. The UAV was launched 5 times during the morning from 7:00 to 10:00 on July 9th to measure the boundary layer dynamics in the early morning and was launched 7 times from 03:50 to 16:30 on July 12th to measure the boundary layer transition from nocturnal boundary layer to the mixing layer. The detailed UAV fights information can be found

in Table 1.

Table 1. Time, altitude, and duration of UAV flights for the experiments on July 9th and July 12th, 2018.

Flight number	Date	Minimum altitude (m a.s.l.)	Maximum altitude (m a.s.l.)	Duration (s)
2018070901	2018.07.09 07:39	90.9	1246.5	709.5
2018070902	2018.07.09 07:48	92.4	1244.8	705.1
2018070903	2018.07.09 08:10	90.9	1243.8	711.7
2018070904	2018.07.09 08:29	89.5	1235.5	691.6
2018070905	2018.07.09 09:34	93.1	1752	1105.5
2018071201	2018.07.12 04:16	91.4	1247.1	701.3
2018071202	2018.07.12 04:31	94.8	1246.1	721.7
2018071203	2018.07.12 07:09	92.7	1246.5	719.6
2018071204	2018.07.12 07:33	93.2	1240.9	717.8
2018071205	2018.07.12 09:44	98.6	1253.7	722.3
2018071206	2018.07.12 14:30	92.8	1248.9	721.3
2018071207	2018.07.12 16:30	92.9	1240.2	716.5

195

Besides, a radiosonde balloon which was operated by the Institute of Energy and Climate Research - Stratosphere (IEK-7) measured the atmospheric parameters from ground to 25 km altitude. COBALD was part of a CFH / ECC ozone / RS41 payload to provide the ~~backscatter~~ backscattering coefficients as well as air temperature, air pressure, relative humidity, ~~and wind~~wind, and ozone concentration with the temporal and spatial resolution being 1s and ~~around~~ about 5 m vertically.

200 The COBALD is a lightweight (500 g) aerosol backscatter detector for balloon-borne measurements developed at the Institute for Atmospheric and Climate Science (ETH Zürich), based on the original approach by Rosen and Kjome (1991). Two light-emitting diodes (LEDs) as light sources and a photodiode detector with a FOV of $6°$ provide high-precision *in-situ* measurements of aerosol backscatter at wavelengths of 455 nm (blue visible) and 940 nm (infrared). COBALD has been originally developed for the observation of high-altitude clouds, such as cirrus (Brabec et al., 2012; Cirisan et al., 2014) and polar

205 stratospheric clouds (Engel et al., 2014), while recently it was proven able to detect and characterize aerosol layers in the upper troposphere–lower stratosphere (Vernier et al., 2015, 2018; Brunamonti et al., 2018, 2021). In this work, we compared COBALD measurements with scanning aerosol LIDAR measurements for validating LIDAR retrievals and investigating the vertical distribution of aerosols. A summary of sensors used on UAV and balloon fights is shown in Table 2.

Table 2. Summary of sensors used on on UAV and balloon fights.

	Measurement	Instrument	Manufacturer	sample flow (lpm)	Time resolution	Mode of operation
UAV						
	Particle size distribution (0.35 - 40 μ m)	OPC-N3	~~Alphasensse~~Alphasensor	5.5	1.6 s	24 size bin
	T, RH	ChipCap2 ~~sensore~~ sensor	Telaire		1s	
	Pressure, wind speed & direction	eBee sensors	AgEagle Aerial Systems Inc.		1 s	
	Lat, lon,				1 s	
Balloon						
	~~Backscatter~~ Backscattering ratio (455 nm & 940 nm)	COBALD	IAC (ETH, Zürich)		1 s	
	Ozone	Electrochemical concentration cell (ECC)	JOSIE (Smit et al., 2007)		1s	
	Water vapor	Cryogenic frostpoint hygrometer (CFH)	EnSci (Vömel et al., 2007; Vömel et al., 2016)		1s	
	Temperature	Vaisala RS41-SGP	Vaisala		1s	
	Altitude, lat, lon & horizontal wind				1s	

3 Results and Discussion

3.1 Comparison of LIDAR data with ground level *in-situ* measurements

The comparison of LIDAR retrievals with ground-level aerosol sizer data was conducted during a field campaign from February 5th to March 5th, 2018 in downtown Stuttgart. In this campaign, the aerosol LIDAR did zenith scans with an elevation angle from 90 ° to 5° in steps of 5°. The nearly horizontal measurement at 5° allows to retrieve extinction coefficients near ground level (from 25 m to 50 m above ground level) by using short-range LIDAR data (ranges: 285 m to 570 m) that can be compared with the ground-level in situ measurements (sampled 3.7 m above ground level). The ground-level *in-situ* aerosol sizer, Fidas200, measured the aerosol size distributions which were used to calculate the aerosol extinction coefficients via Mie code. Figure 2 shows the extinction coefficients retrieved from LIDAR measurements and from Mie calculations based on aerosol size distribution (labeled as "Raw size distribution"). The extinction coefficients obtained from LIDAR were both retrieved from the slope and Raman retrieval methods (Seidel et al., 2010; Ansmann et al., 1992). In the slope and Raman
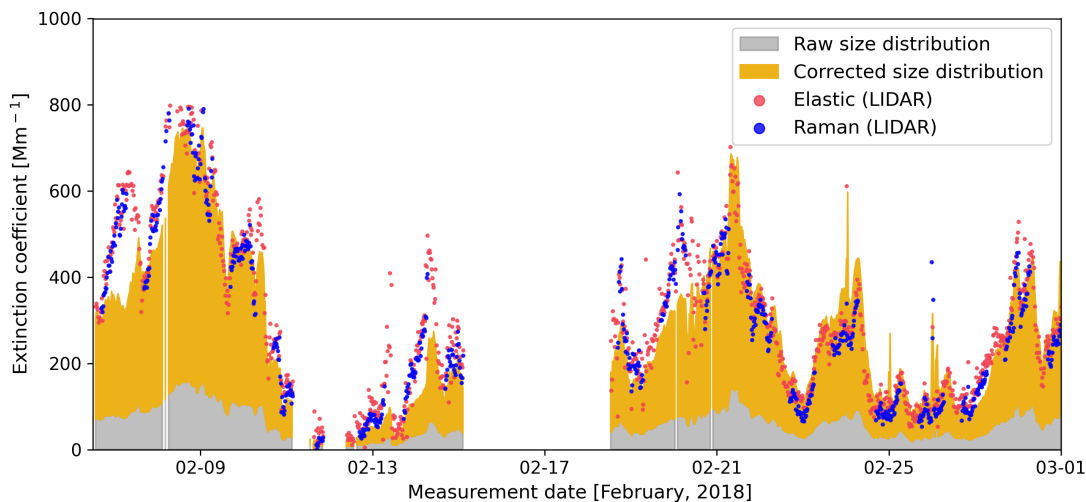
Figure 2. Time series of ground-level extinction coefficients retrieved from LIDAR measurements (both elastic and Raman methods) ~~,~~ and from Mie ~~calculation~~ calculations based on OPC raw size ~~distribution~~ distributions as well as size ~~distribution~~ distributions corrected by counting efficiency ~~and hygroscopic effect~~ from February 5th to March 5th, 2018 in downtown Stuttgart.

220   retrieval methods, a linear regression was used and the correlation coefficients of linear regressions are 0.99 ± 0.05 and 0.99 ± 0.06 for slope and Raman retrieval methods, respectively. This is also an indication for a rather homogeneous distribution of the aerosol particles within the altitude range from 25 to 50 m corresponding to a range between 285 and 570 m. This figure shows that the ~~raw~~ extinction coefficients from Mie calculations based on raw OPC size distributions are systematically lower than those from LIDAR retrievals by a factor of 4.70 ± 1.49. The reason for this phenomenon is that the Fidas200 underestimates

225   the particle number by a factor of 2-10 at ~~a diameter~~ diameters between 0.25 μm and 0.5 μm when compared with SMPS data as shown in Figure S1. The left side of Figure S1 shows the number size distribution from Fidas200 and the merged size distribution from SMPS and APS measurements. ~~From this figure, we can see that Fidas200 underestimated particle number size distributions at a diameter between 0.25 μm and 0.5 μm when compared with the merged size distribution (called "loss effect").~~ The right plot of ~~this figure~~ Figure S1 shows the accumulated extinction coefficients calculated from Mie theory based

230   on those two size distributions, which shows ~~that the underestimation of particle numbers from 0.25 μm to 0.5 μm causes the modelled extinction from the Fidas200 size distributions to be lower than that modelled from merged size distribution~~ the substantial difference by a factor of ~~around 4.~~ four. Hence, we conclude that the underestimation of particle ~~number~~ numbers from 0.25 μm to 0.5 μm is one of the main reasons for the underestimation of extinction coefficients based on ~~OPC data alone~~uncorrected OPC data.

235

~~The systematic underestimation of aerosol particle number from 0.25 μm to 0.5 μm allows for calculating a counting efficiency curve as shown in~~ Based on systematic laboratory measurements with the different particle sizers Fidas200 OPC, SMPS, and APS the FIDAS200 counting efficiency was determined (see Figure S2. ~~Then the calculated counting efficiency curve~~
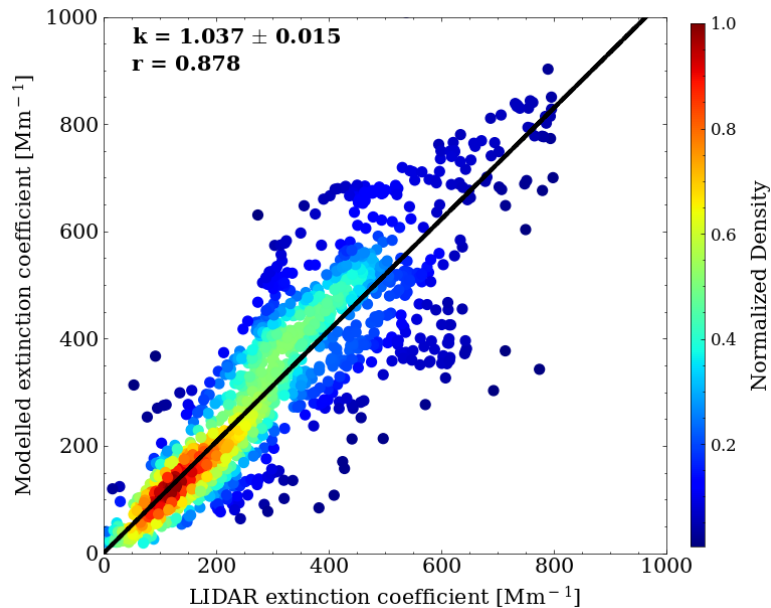
Figure 3. Correlation of extinction coefficients from LIDAR retrieval and Mie calculation from February 5th to March 5th, 2018 in Stuttgart. The relative humidity used in the model is container indoor relative humidity and the black line is the regression fitting curve of them. The red line is the regression fitting curve between the LIDAR-derived extinction coefficients and those from Mie calculation by using ambient relative humidity.

240 ~~was applied to the Fidas200 size distribution to get a corrected aerosol size distribution. This corrected size distribution is~~). This counting efficiency was used to correct all measured size distributions. The corrected size distributions were used to calculate the ~~corrected~~ extinction coefficients via Mie calculation. The time series of the ~~corrected~~ extinction coefficients calculated from the corrected size distribution is shown in Figure 2 ~~. The orange areaindicates the extinction coefficients due to the underestimation of aerosol particle number from 0.25 µm to 0.5 µm. After taking into account the particle number underestimation, the modelled extinction coefficient shows good agreement with~~ (orange area). The calculated extinction

245 coefficients show a reasonable agreement with the LIDAR retrievals. ~~Although good agreement between *in-situ* and LIDAR measurements, the aerosol hygroscopic growth effect is still not considered. The modelled extinction coefficients contributed by aerosol hygroscopic growth are labeled as "hygroscopicity (container)" and "hygroscopicity (Ambient)" in Figure 2, representing the relative humidity used in the model are container indoor relative humidity and ambient relative humidity, respectively. The~~ The correlation plot between the extinction coefficient ~~for container indoor relative humidity~~ from Fidas 200 and the LIDAR-

250 derived extinction coefficient is shown in Figure 3, which shows a slope and a Pearson correlation coefficient of 1.037 ± 0.015 and 0.878, respectively. ~~The dashed line in this figure is the regression fitting curve between the LIDAR-derived extinction coefficients and those from Mie calculation by using ambient relative humidity, which shows a slope and a Pearson correlation coefficient of 1.463 ± 0.025 and 0.845, respectively.~~ As shown in ~~these two figures~~Figure 2, the extinction coefficients retrieved

from LIDAR measurement show a similar trend ~~for both extinction coefficients but shows better agreement with the one~~ with those calculated based on ~~the container indoor relative humidity. The reason for a better agreement based on the indoor relative humidity instead of~~ corrected Fidas 200 size distributions. Please note, that the extinction coefficient based on Fidas 200 data are still a little lower than those based on lidar measurements. This may be caused by a partial loss of water from the aerosol particles due to higher temperatures inside the container. However, the ~~outdoor ambient relative humidity is due to the fact that the~~ aerosol particles ~~lost their water partly inside the container but did not~~ are not expected to reach equilibrium within the residence time of 3 ~~s residence time~~ seconds in the sampling line inside the warm container. Please note, that there was no dryer in the sampling line~~and the impact of the relative humidity correction on our comparison is much smaller than the correction of the size measurements.~~. From the fraction of extinction coefficients shown in Figure 2, we can determine that the main reason for causing extinction coefficient inconsistency between *in-situ* measurement and LIDAR retrieval is the undercounting by the ~~OPC.~~ Fidas 200. The relatively good agreement of the extinction coefficients after our reasonable corrections reflects the reliability of our methods and the good quality of the LIDAR retrievals.

3.2   Comparison of LIDAR data with *in-situ* measurements on a UAV

The comparison of LIDAR and UAV measurements was conducted for two days, on July 9th and July 12th, 2018 to study the vertical distribution of aerosols and the boundary layer structure. The sky was almost free of clouds during UAV flights on July 9th while it was affected by clouds within the boundary layer on July 12nd.

Figure 4 shows the time series of ~~backscatter coefficientsand boundary layer~~ backscattering coefficients, boundary layer heights (pink squares) and residual layer heights (yellow squares) retrieved from LIDAR measurement (pink squares) as well as boundary layer ~~height~~ heights (a.s.l. - above see level) obtained from UAV measurements (black star with white circle surrounded) and from ERA5 ~~dataset (white dashed line) and potential temperatures obtained from UAV measurements (white solid~~ dataset (white dashed line) on July 9th, 2018. This figure shows that the boundary layer height retrieved from the LIDAR measurement is consistent with the boundary layer height from the UAV measurement ~~(the maximum gradient of potential temperature)~~ which both show an increasing trend of the boundary layer during the morning of this day. In addition, the boundary layer from ERA5 also shows a similar trend as the observations but overestimates boundary layer height, especially during daytime. A possible reason for this overestimation is that the existence of clouds during daytime reduced solar radiation and a low value of solar radiation caused a shallow boundary layer at this time. Figure 4 also shows a stable nocturnal boundary layer and a residual layer during nighttime measured by scanning aerosol LIDAR. The low and stable boundary at night time can suppress the dispersion of aerosol near the surface. Hence, the ~~backscatter~~ backscattering coefficients within the boundary layer are maximum (highest aerosol concentration) during the morning rush hour due to the combined effect of the shallow boundary layer and local anthropogenic emissions. After sunrise, the convection became stronger, which caused an increase of the boundary layer height and dilution of aerosols within the boundary layer, so the aerosol concentrations within the boundary layer decreased. Figure ~~??~~ S3 shows the time series of range-corrected LIDAR signal and boundary layer heights retrieved from LIDAR as well as boundary layer ~~height obtained from~~ heights obtained from UAV measurement (black star with white
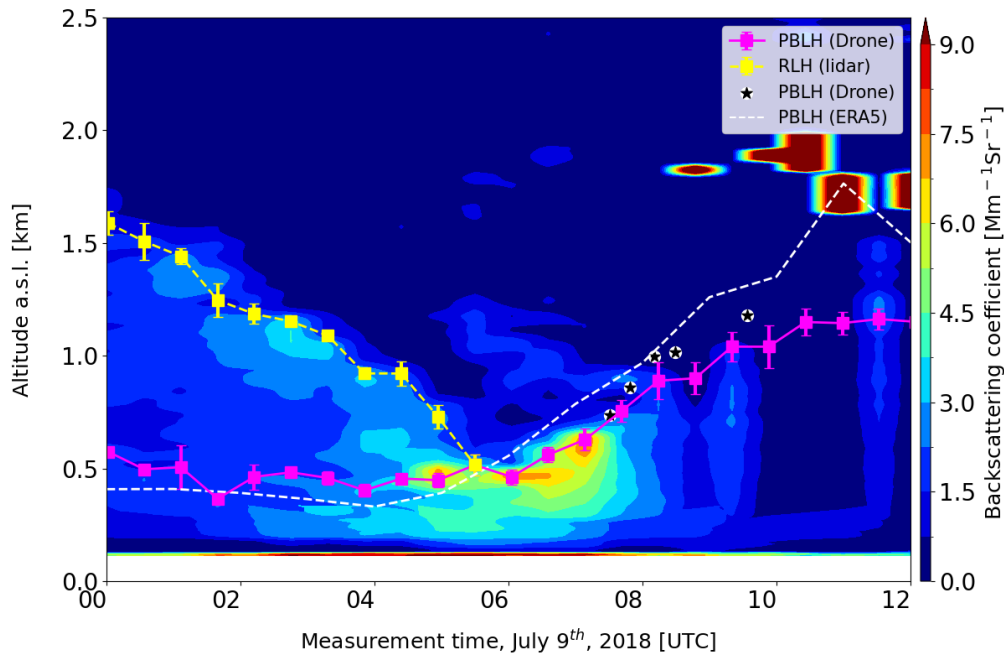
Figure 4. Time series of ~~backscatter~~ backscattering coefficients (contour), boundary layer ~~height~~ heights (PBLH, pink squares) and residual layer ~~retrieved~~ heights (RLH, yellow squares) retrieved from scanning LIDAR, as well as boundary layer heights obtained from ~~ERA5 dataset~~ UAV measurements (black star with white ~~dashed line~~circle surrounded) and ~~vertical potential temperature profiles~~ from ERA5 dataset (white ~~solid~~ dashed line) measured by UAV on July 9th, 2018.

circle surrounded) and from ERA5 ~~dataset (white dash line) and potential temperature obtained from UAV measurements (white solid~~ dataset (white dash line) on July12^{th}, 2018. The reason for showing range-corrected LIDAR signal instead of 290 ~~backscatter~~ backscattering coefficients is that low-level clouds prevented retrieving the ~~backscatter~~ backscattering coefficients from range-corrected LIDAR signal by the Klett-Fernald method. This figure also shows consistency in boundary layer heights among LIDAR, UAV, and ERA5. More interestingly, the cloud existed at the top of the boundary layer from 05:00 to 13:00 and the cloud base increased with boundary layer height as captured by the LIDAR measurements. The reason for the cloud existing on the top of the boundary layer is that the relative humidity has a maximum value at the top of the boundary layer 295 in the well-mixing boundary layer and this high relative humidity ambient environment provided a good conditions for cloud formation. Figure ~~S3~~ S4 shows the correlation of boundary layer heights from LIDAR and radiosonde retrievals for both two days, which show a good correlation with a slope of 1.01 ± 0.24 and a Pearson correlation coefficient of 0.793.
~~Time series of range corrected LIDAR signal and boundary layer height retrieved from scanning LIDAR (pink squares) as well as boundary layer heights obtained from ERA5 dataset (white dashed line) and vertical potential temperature profiles (white~~ 300 ~~solid line) measured by UAV on July 12th, 2018.~~

A comparison of the vertical profile of aerosols from LIDAR and UAV measurements was conducted in the following steps.
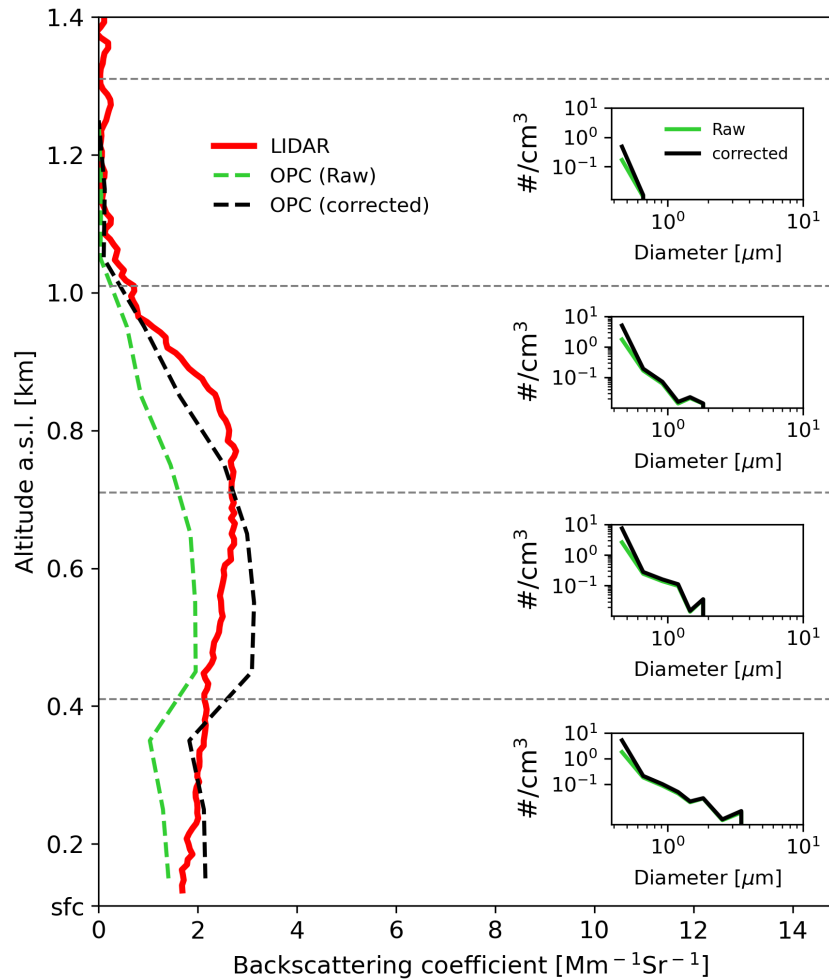
Figure 5. Vertical distribution of ~~backscatter~~ backscattering coefficients from LIDAR measurement (solid red line, averaged from 08:14 - 08:25), as well as ~~backscatter~~ backscattering coefficients derived from UAV-based measurements for raw size distributions (dashed green line), and corrected particle size distributions (dashed black line) (inserts on the right) on July 9th, 2018. Note: The 'sfc' on the y-axis indicates ground surface level.

First, we used the temperature and pressure measured by UAV instead of an atmospheric model to calculate molecular ~~backscatter~~ backscattering coefficients, and these molecular ~~backscatter~~ backscattering profiles were used for LIDAR retrievals. Second, the ~~backscatter~~ backscattering coefficients at all observation angles were calculated using the Klett-Fernald method with reference values obtained from vertical profiles of the ~~backscatter~~ backscattering coefficients. Finally, Mie theory was used to calculate the aerosol ~~backscatter~~ backscattering coefficients based on size distributions measured by the UAV-borne OPC and the complex refractive index from a nearby sun photometer. As there are no dryer before OPC-N3 sampling and

no temperature difference between sampling tube and ambient environment, the effect of relative humidity on aerosol sampling was not considered. Figure 5 shows the backscattering coefficients retrieved from LIDAR measurements and from Mie calculations based on size distributions measured by the OPC on the UAV. In this experiment, the LIDAR performed zenith scans using elevation angles from 90° to 5° with steps of 5° during the UAV flights. Consequently, we retrieve the backscattering coefficients for each observation angle and the average of these backscattering coefficients is shown as thick red line to compare with the UAV measurements. The average time is around 11 minutes for lidar measurement from 08:14 - 08: 25 on July 09, 2018. This figure shows that the vertical distribution of the aerosol particles in the well-mixed boundary layer is reflected well in both LIDAR and OPC measurements. Furthermore, the backscattering coefficients from UAV retrievals (green dashed line in figure 5) show the same aerosol mixing height and the same order of backscattering coefficients as LIDAR retrievals. The smaller backscattering coefficients calculated based on airborne OPC measurements may be related to an undercounting of the smaller particles as we have seen for ground based OPC measurements by the Fidas 200 instrument. The size distributions were corrected by the counting efficiency curve introduced in section 3.1. The backscattering coefficients from corrected size distributions (black dashed line in figure 6) were consistent with the lidar-derived backscattering coefficients. Although Fidas200 is a different OPC sensor as OPC-N3, the same undercounting phenomenon was observed for both sensors. Please note that the particle size is averaged over 300 m and the horizontal dashed lines represent these average altitude ranges. These vertical size distributions show that larger particles were detected only below 300 m above ground level.

12 UAV flights were conducted on July 9th and July 12th as shown in Table 1 to compare with LIDAR retrievals. Figure 6 shows the correlation of backscattering coefficients retrieved from LIDAR measurement and from Mie calculation based on aerosol size distributions measured by OPC-N3 on the UAV. The data from LIDAR and UAV was averaged into 60 m vertical bins to reduce the noise of the OPC-N3 measurement. The colours of the scatter points indicated different UAV flights. This figure shows that the backscattering coefficients retrieved from LIDAR correlated on average with the backscattering coefficients calculated from the OPC with a slope of 0.789 ± 0.096 and a Pearson correlation coefficient of 0.234. This figure also shows that 75% of data points are within the grey shaded area, which indicates that these data are within a factor of 3. However, in contrast to the ground level OPC measurements a dedicated correction of the low cost OPC data for potential sampling artefacts or undercounting was not possible. This figure also shows that the UAV measurements reflect the same aerosol mixing process within the boundary layer and the same order of magnitude of the backscattering coefficient. However, the backscatter coefficients retrieved from the UAV-borne OPC in certain UAV flights still show a relatively large deviation from LIDAR retrievals. One reason for this variability is that the UAV cruising speed may affect aerosol sampling by the OPC-N3. The sample were collected perpendicular to the flight direction into the OPC, so we can expect size-dependent discrimination of larger particles. Compared to the Fidas200 OPC as shown in section 3.1, the OPC-N3 data show a significantly higher variability. This means that we must be careful with the quality and the operation of such *in-situ* measurements especially when no reference data like lidar are available.
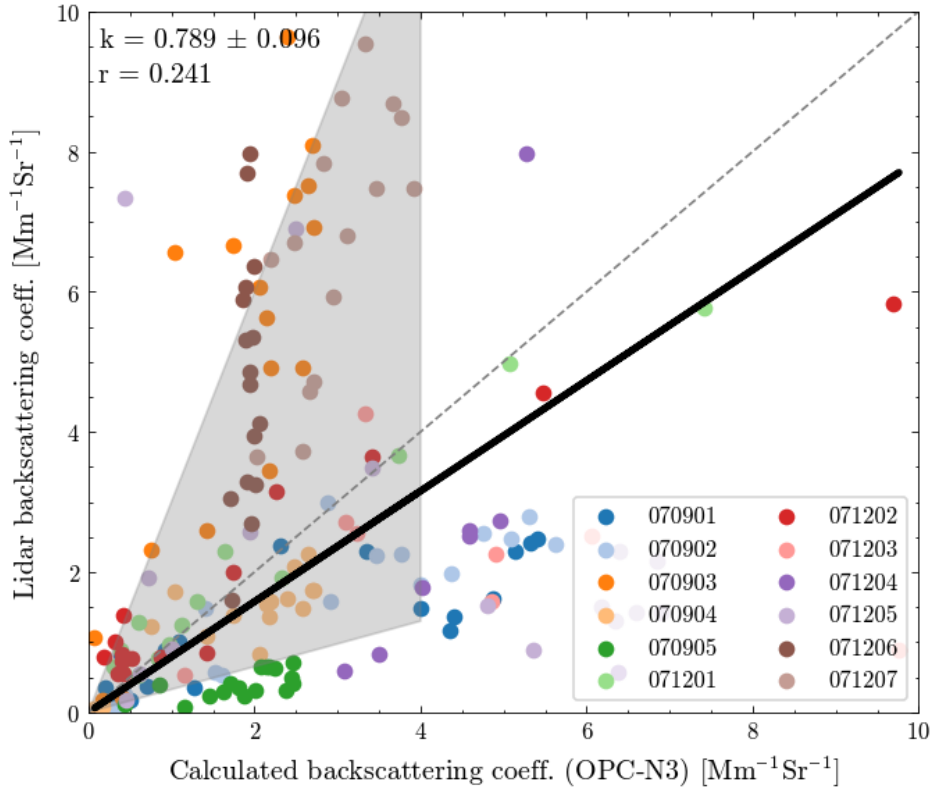
Figure 6. Correlation of ~~backscatter~~ backscattering coefficients retrieved from LIDAR measurement and modelled from Mie calculation based on aerosol size distribution measured by OPC-N3 on the UAV for all UAV flights on July 9th and July 12th, 2018. The different scatter point colours indicates different UAV flights. The thick black line is a linear fit to the data and the thin dashed line is the 1:1 line

3.3 Comparison of LIDAR data with *in-situ* measurements onboard a balloon

A balloon which carried the COBALD sensor to measure ~~backscatter~~ backscattering coefficients *in-situ* was launched to an
345   altitude of around 30 km on the night of July 12th, 2018 to validate LIDAR retrievals. The LIDAR did vertically pointed measurements with an integration time of 60 s for each profile during the balloon launch. Figure 7a shows the range corrected LIDAR signal for two hours of continuous measurement and the vertical trajectory of the balloon. As shown in this figure, the LIDAR signal did not vary much in the first hour (the period was highlighted in this figure) while showing changes in the second half of the experiment. Hence, we selected the first hour to compare with balloon measurements. Figure 7b
350   shows the horizontal trajectory of the radiosonde with the colour of the plot indicating the radiosonde altitude and the circle indicating the distance from the LIDAR observation station. This figure shows that the horizontal displacement of the radiosonde is about 10 km when the radiosonde reached an altitude of 10 km and this horizontal displacement may cause a difference in ~~backscatter~~ backscattering coefficients between LIDAR and COBALD. For the LIDAR analysis in this experiment, the ~~backscatter~~ backscattering coefficients were retrieved from elastic and Raman data with the vertical profiles of the

molecular ~~backscatter~~ backscattering coefficient being calculated from temperature and pressure measured by the balloon. The COBALD data analysis follows the procedure proposed by Brunamonti et al. (2021). First, a wavelength extrapolation yielded the ~~backscatter~~ backscattering coefficient at a wavelength of 355 nm from COBALD measurement. The Ångström exponent (AE) used for this wavelength conversion is measured by COBALD at two wavelengths (455 nm & 940 nm) and extended to the wavelength of 355 nm. Second, as the Field of View (FOV) of LIDAR and COBALD are different (the FOV of COBALD is 6° whereas the FOV of LIDAR is 2.3 mrad), a FOV correction is necessary. The correction factors are calculated based on Mie theory and are shown in Figure 2 in Brunamonti et al. (2021).

Figure 8 shows the ~~backscatter~~ backscattering coefficients from COBALD and LIDAR measurement for a LIDAR integration time of 1 hour. These two profiles of ~~backscatter~~ backscattering coefficients from LIDAR are retrieved from elastic and Raman channel data respectively. The retrieval of ~~backscatter~~ backscattering coefficients from elastic channel data remained with larger uncertainty due to the assumption of a LIDAR ratio in the Klett-Fernald method. Hence, it is more meaningful to compare ~~backscatter~~ backscattering coefficients from Raman data with those from COBALD measurements. In addition, the volume and particle depolarization ratios measured by LIDAR are shown on the right side of Figure 8. The low depolarization ratios support our assumption that the particles are spherical and that we can use Mie calculations for the FOV correction. This figure shows a good agreement in ~~backscatter~~ backscattering coefficients between LIDAR Raman data retrieval and COBALD measurement at an altitude above 2 km. However, there is a significant discrepancy at altitudes below 2 km.

The discrepancy of the ~~backscatter~~ backscattering coefficients between LIDAR retrievals and COBALD measurements at lower altitudes is due to the temporal evolution of aerosol particle concentrations in the boundary layer as can be seen from vertical profiles of ~~backscatter~~ backscattering coefficients with high temporal resolution in Figure ~~S4~~S5. This figure shows profiles of ~~backscatter~~ backscattering coefficients retrieved from LIDAR Raman data with 5 - minute temporal resolution and ~~backscatter~~ backscattering coefficients measured by COBALD as well as the vertical balloon trajectory. This figure shows a good agreement in ~~backscatter~~ backscattering coefficients between COBALD measurement and LIDAR Raman data retrievals at the
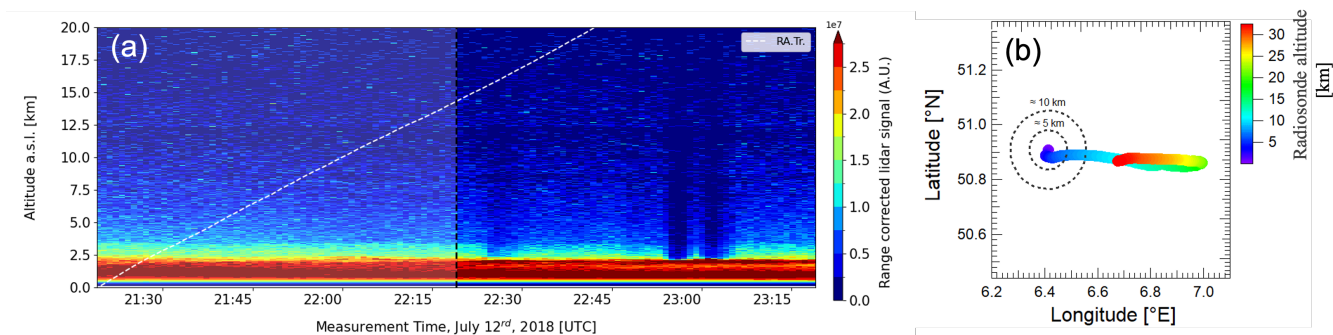
Figure 7. Time series of range corrected LIDAR signal and radiosonde vertical trajectory (white dash line) (a) and ~~Horizontal~~ horizontal displacement of the balloon during this experiment (b) on July 12th, 2018 at Jülich research center.
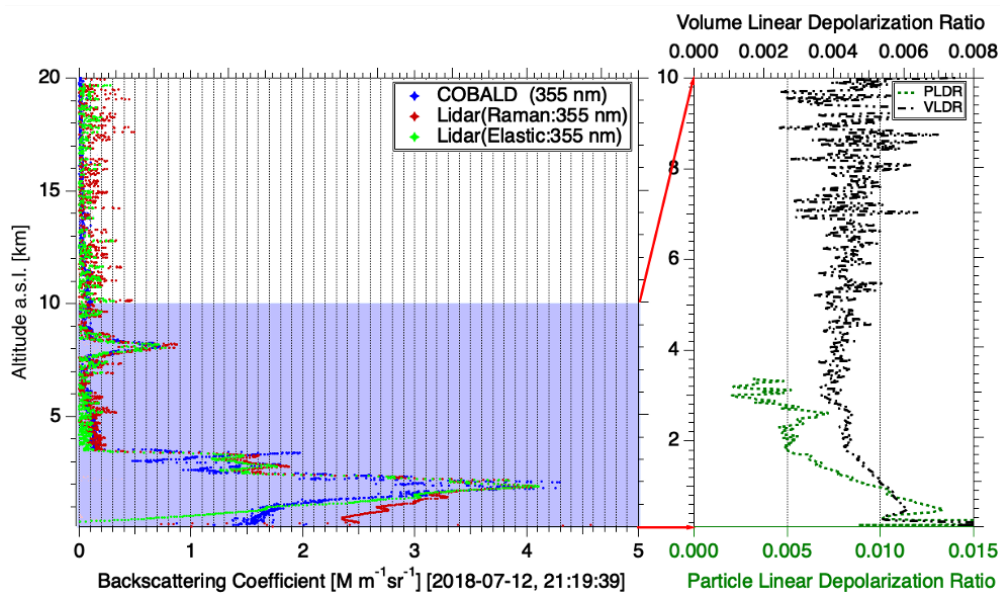
Figure 8. Backscatter coefficients measured by balloon-borne COBALD and LIDAR (left) as well as aerosol volume and particle depolarization ratio measured by LIDAR (right) on the night time of July 12th, 2018 at Jülich research center. (The integration time of the LIDAR data is 1 hour from 21:19 to 22:19.)

altitude of the balloon passing by. The ~~backscatter~~ backscattering values at the altitude of the balloon passing by are extracted as shown as the red line in Figure ~~S4~~ S5 to obtain merged Raman ~~backscatter~~ backscattering coefficients. The merged Raman ~~backscatter coefficients and backscatter~~ backscattering coefficients and backscattering coefficients from COBALD measure-
380 ments are shown on the left side of Figure 9, showing very good agreement of ~~backscatter~~ backscattering coefficients from LI-DAR and COBALD measurements at all altitudes. The correlation between LIDAR merged Raman ~~backscatter~~ backscattering coefficients and COBALD ~~backscatter~~ backscattering coefficients is shown on the right side of Figure 9, which shows these two ~~backscatter~~ backscattering coefficients are well correlated with a slope of 1.063 ± 0.016 and a Pearson correlation coefficient of 0.925. This consistency between LIDAR and COBALD sensor reflects a good data quality of both methods and proves that
385 LIDAR can provide reliable and vertical profiles of aerosol particles with high spatial-temporal resolution.
~~Profiles of backscatter coefficients from LIDAR for integration over 1 hour (grey dash line) and sliding 5-minute merged backscatter coefficients (green line) as well as the vertical profile of *in-situ* backscatter coefficient measured by balloon-borne COBALD (blue line) on July 12th, 2018 at the Jülich research center (left). Correlation between LIDAR merged backscatter coefficients and balloon-borne COBALD backscatter coefficients (right).~~
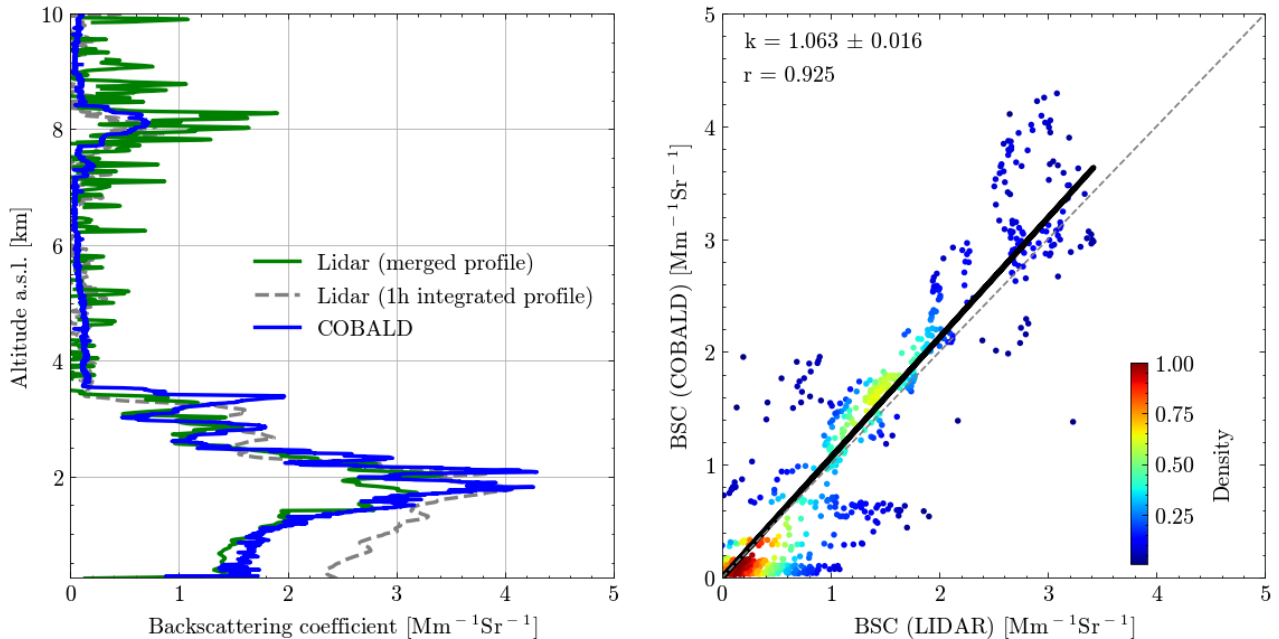
Figure 9. Profiles of backscattering coefficients from LIDAR for integration over 1 hour (grey dash line) and sliding 5-minute merged backscattering coefficients (green line) as well as the vertical profile of *in-situ* backscattering coefficient measured by balloon-borne COBALD (blue line) on July 12th, 2018 at the Jülich research center (left). Correlation between LIDAR merged backscattering coefficients and balloon-borne COBALD backscattering coefficients (right).

4 Conclusions

This paper presents results of aerosol spatial-temporal distribution and optical properties measured by a scanning aerosol LIDAR, a radiosonde with a backscatter sensor, an OPC-N3 on a UAV, and a comprehensive set of ground level *in-situ* measurements. Modern aerosol characterisation methods including remote sensing and *in-situ* methods helped us better understand the aerosol physical properties and build a bridge between remote sensing and these *in-situ* methods. This paper focuses on the comparison of aerosol measurement between LIDAR retrievals and *in-situ* measurements at ground level, in the troposphere, and in the stratosphere, thus validating LIDAR retrievals at all altitude levels.

The comparison of ground-level *in-situ* extinction coefficients with LIDAR-derived ones shows that Fidas200 underestimated particle number concentration by a factor of 2-10 at the diameter range between 0.25 μm and 0.5 μm, thus causing the total extinction calculated from this size distribution to be systematically lower than that from LIDAR retrievals by a factor of 4.70 $\pm$ 1.49. The extinction coefficient calculated from the Fidas200 aerosol size distribution corrected by SMPS size distribution shows good agreement with LIDAR-derived extinction coefficient with a slope of 1.037 $\pm$ 0.015 and a Pearson correction coefficient of 0.878. The comparison also shows that the undercounting of aerosol particles between 0.25 μm and 0.5 μm is the main reason for the large discrepancy between LIDAR retrieval and ground-level *in-situ* Fidas200 measurements. In

addition, a comparison between LIDAR and UAV shows good agreement in boundary layer height measurements and both methods show a similar trend as the ERA5 boundary layer height evolution. The OPC-N3 aboard UAV shows a similar aerosol vertical distribution and comparable ~~backscatter~~ backscattering coefficients as LIDAR measurement. However, the ~~backscatter~~ backscattering coefficients calculated from OPC-N3 were unstable and large uncertainties still remained for different flights most likely due to the effect of UAV cruising on OPC-N3 sampling. Adapting the inlet design of the OPC may improve the data quality for future measurements. Finally, the backscatter from balloon-borne COBALD measurement shows very good agreement with the backscatter retrieved from LIDAR measurement if compared with 5-minute resolution LIDAR data with a slope of 1.063 ± 0.016 and a Pearson correlation coefficient of 0.925. This consistency between LIDAR and COBALD sensor validated our LIDAR retrievals and proves that LIDAR can provide reliable and high-resolution vertical profiles of aerosols. And this comparison highlights the complementary advantages of lidar's continuous measurement capability and COBALD *in-situ* two wavelength data for characterising aerosol particles from near ground level up to the stratosphere. In conclusion, the retrievals from scanning aerosol LIDAR measurements show good agreement with *in-situ* measurements at all altitude levels and these LIDAR measurements can also used as reference for other low cost in-situ measurements.

Code availability. The code used to analyse the LIDAR data is property of Raymetrics Inc, but we have shown that it gives the same results as the code "single calculus chain" (SCC) provided by EARLIENT https://www.earlinet.org/index.php?id=earlinet_homepage, last access: 14 February 2023 and public available. The Mie code used in this paper is available via github repository https://github.com/jleinonen/pymiecoated, last access: 14 February 2023.

Data availability. The LIDAR raw data and ground *in-situ* data are available via the open access data repository KITopen (link to be added). The UAV data and balloon data are available via the open access data repository Jülich DATA (link to be added).

Author contributions. CR, RT, CW, and HS performed the measurements and analyzed *in-situ* measurement data. HZ analysed the LIDAR remote sensing data. FGW post-processed the COBALD data. HZ wrote the manuscript with support from HS as well as contributions from all co-authors.

Competing interests. The authors declare that they have no conflict of interest.

Acknowledgements. Support by the staff of the Institute of Meteorology and Climate Research and the Institute of Energy and Climate Research (FZJ), financial support by the project Modular Observation Solutions for Earth Systems (MOSES) of the Helmholtz Association (HGF).

References

Predicting forest fire in the Brazilian Amazon using MODIS imagery and artificial neural networks, International Journal of Applied Earth Observation and Geoinformation, 11, 265–272, https://doi.org/10.1016/j.jag.2009.03.003, 2009.

Adam, M., Nicolae, D., Stachlewska, I. S., Papayannis, A., and Balis, D.: Biomass burning events measured by lidars in EARLINET – Part 1: Data analysis methodology, Atmospheric Chemistry and Physics, 20, 13 905–13 927, https://doi.org/10.5194/acp-20-13905-2020, 2020.

Alam, K., Trautmann, T., and Blaschke, T.: Aerosol optical properties and radiative forcing over mega-city Karachi, Atmospheric Research, 101, 773–782, https://doi.org/10.1016/j.atmosres.2011.05.007, international Conference on Nucleation and Atmospheric Aerosols (Part 2), 2011.

Althausen, D., Müller, D., Ansmann, A., Wandinger, U., Hube, H., Clauder, E., and Zörner, S.: Scanning 6-wavelength 11-channel aerosol lidar, Journal of Atmospheric and Oceanic Technology, 17, 1469–1482, https://doi.org/10.1175/1520-0426(2000)017<1469:SWCAL>2.0.CO;2, 2000.

Anderson, T., Covert, D., Marshall, S., Laucks, M., Charlson, R., Waggoner, A., Ogren, J., Caldow, R., Holm, R., Quant, F., et al.: Performance characteristics of a high-sensitivity, three-wavelength, total scatter/backscatter nephelometer, Journal of Atmospheric and Oceanic Technology, 13, 967–986, https://doi.org/10.1175/1520-0426(1996)013<0967:PCOAHS>2.0.CO;2, 1996.

Ansmann, A., Wandinger, U., Riebesell, M., Weitkamp, C., and Michaelis, W.: Independent measurement of extinction and backscatter profiles in cirrus clouds by using a combined Raman elastic-backscatter lidar, Applied optics, 31, 7113–7131, https://doi.org//10.1364/AO.31.007113, 1992.

Avdikos, G.: Powerful Raman Lidar systems for atmospheric analysis and high-energy physics experiments, in: EPJ Web of Conferences, vol. 89, p. 04003, EDP Sciences, https://doi.org/10.1051/epjconf/20158904003, 2015.

Baars, H., Ansmann, A., Engelmann, R., and Althausen, D.: Continuous monitoring of the boundary-layer top with lidar, Atmospheric Chemistry and Physics, 8, 7281–7296, https://doi.org/10.5194/acp-8-7281-2008, 2008.

Baars, H., Kanitz, T., Engelmann, R., Althausen, D., Heese, B., Komppula, M., Preißler, J., Tesche, M., Ansmann, A., Wandinger, U., Lim, J.-H., Ahn, J. Y., Stachlewska, I. S., Amiridis, V., Marinou, E., Seifert, P., Hofer, J., Skupin, A., Schneider, F., Bohlmann, S., Foth, A., Bley, S., Pfüller, A., Giannakaki, E., Lihavainen, H., Viisanen, Y., Hooda, R. K., Pereira, S. N., Bortoli, D., Wagner, F., Mattis, I., Janicka, L., Markowicz, K. M., Achtert, P., Artaxo, P., Pauliquevis, T., Souza, R. A. F., Sharma, V. P., van Zyl, P. G., Beukes, J. P., Sun, J., Rohwer, E. G., Deng, R., Mamouri, R.-E., and Zamorano, F.: An overview of the first decade of Polly[NET]: an emerging network of automated Raman-polarization lidars for continuous aerosol profiling, Atmospheric Chemistry and Physics, 16, 5111–5137, https://doi.org/10.5194/acp-16-5111-2016, 2016.

Bahreini, R., Jimenez, J. L., Wang, J., Flagan, R. C., Seinfeld, J. H., Jayne, J. T., and Worsnop, D. R.: Aircraft-based aerosol size and composition measurements during ACE-Asia using an Aerodyne aerosol mass spectrometer, Journal of Geophysical Research: Atmospheres, 108, https://doi.org/10.1029/2002JD003226, 2003.

Böckmann, C., Wandinger, U., Ansmann, A., Bösenberg, J., Amiridis, V., Boselli, A., Delaval, A., De Tomasi, F., Frioud, M., Grigorov, I. V., et al.: Aerosol lidar intercomparison in the framework of the EARLINET project. 2. Aerosol backscatter algorithms, Applied Optics, 43, 977–989, 2004.

Bohren, C. F. and Huffman, D. R.: Absorption and scattering of light by small particles, John Wiley & Sons, 2008.

465   Brabec, M., Wienhold, F. G., Luo, B. P., Vömel, H., Immler, F., Steiner, P., Hausammann, E., Weers, U., and Peter, T.: Particle backscatter and relative humidity measured across cirrus clouds and comparison with microphysical cirrus modelling, Atmospheric Chemistry and Physics, 12, 9135–9148, https://doi.org/10.5194/acp-12-9135-2012, 2012.

Brunamonti, S., Jorge, T., Oelsner, P., Hanumanthu, S., Singh, B. B., Kumar, K. R., Sonbawne, S., Meier, S., Singh, D., Wienhold, F. G., Luo, B. P., Boettcher, M., Poltera, Y., Jauhiainen, H., Kayastha, R., Karmacharya, J., Dirksen, R., Naja, M., Rex, M., Fadnavis, S., and Peter, T.:
470   Balloon-borne measurements of temperature, water vapor, ozone and aerosol backscatter on the southern slopes of the Himalayas during StratoClim 2016–2017, Atmospheric Chemistry and Physics, 18, 15 937–15 957, https://doi.org/10.5194/acp-18-15937-2018, 2018.

Brunamonti, S., Martucci, G., Romanens, G., Poltera, Y., Wienhold, F. G., Hervo, M., Haefele, A., and Navas-Guzmán, F.: Validation of aerosol backscatter profiles from Raman lidar and ceilometer using balloon-borne measurements, Atmospheric Chemistry and Physics, 21, 2267–2285, https://doi.org/10.5194/acp-21-2267-2021, 2021.

475   Burton, S. P., Ferrare, R. A., Hostetler, C. A., Hair, J. W., Rogers, R. R., Obland, M. D., Butler, C. F., Cook, A. L., Harper, D. B., and Froyd, K. D.: Aerosol classification using airborne High Spectral Resolution Lidar measurements – methodology and examples, Atmospheric Measurement Techniques, 5, 73–98, https://doi.org/10.5194/amt-5-73-2012, 2012.

Burton, S. P., Vaughan, M. A., Ferrare, R. A., and Hostetler, C. A.: Separating mixtures of aerosol types in airborne High Spectral Resolution Lidar data, Atmospheric Measurement Techniques, 7, 419–436, https://doi.org/10.5194/amt-7-419-2014, 2014.

480   Ceolato, R. and Berg, M. J.: Aerosol light extinction and backscattering: A review with a lidar perspective, Journal of Quantitative Spectroscopy and Radiative Transfer, 262, 107 492, 2021.

Cheng, K.-C., Acevedo-Bolton, V., Jiang, R.-T., Klepeis, N. E., Ott, W. R., Fringer, O. B., and Hildemann, L. M.: Modeling exposure close to air pollution sources in naturally ventilated residences: Association of turbulent diffusion coefficient with air change rate, Environmental science & technology, 45, 4016–4022, https://doi.org/10.1021/es103080p, 2011.

485   Cirisan, A., Luo, B. P., Engel, I., Wienhold, F. G., Sprenger, M., Krieger, U. K., Weers, U., Romanens, G., Levrat, G., Jeannet, P., Ruffieux, D., Philipona, R., Calpini, B., Spichtinger, P., and Peter, T.: Balloon-borne match measurements of midlatitude cirrus clouds, Atmospheric Chemistry and Physics, 14, 7341–7365, https://doi.org/10.5194/acp-14-7341-2014, 2014.

Drinovec, L., Močnik, G., Zotter, P., Prévôt, A. S. H., Ruckstuhl, C., Coz, E., Rupakheti, M., Sciare, J., Müller, T., Wiedensohler, A., and Hansen, A. D. A.: The "dual-spot" Aethalometer: an improved measurement of aerosol black carbon with real-time loading compensation,
490   Atmospheric Measurement Techniques, 8, 1965–1979, https://doi.org/10.5194/amt-8-1965-2015, 2015.

Düsing, S., Wehner, B., Seifert, P., Ansmann, A., Baars, H., Ditas, F., Henning, S., Ma, N., Poulain, L., Siebert, H., et al.: Helicopter-borne observations of the continental background aerosol in combination with remote sensing and<? xmltex\break?> ground-based measurements, Atmospheric Chemistry and Physics, 18, 1263–1290, https://doi.org/10.5194/acp-18-1263-2018, 2018.

Engel, I., Luo, B. P., Khaykin, S. M., Wienhold, F. G., Vömel, H., Kivi, R., Hoyle, C. R., Grooß, J.-U., Pitts, M. C., and Peter, T.: Arctic strato-
495   spheric dehydration – Part 2: Microphysical modeling, Atmospheric Chemistry and Physics, 14, 3231–3246, https://doi.org/10.5194/acp-14-3231-2014, 2014.

Fernald, F. G.: Analysis of atmospheric lidar observations: some comments, Appl. Opt., 23, 652–653, https://doi.org/10.1364/AO.23.000652, 1984a.

Fernald, F. G.: Analysis of atmospheric lidar observations: some comments, Appl. Opt, 23, 652–653, 1984b.

500   Ferrero, L., Ritter, C., Cappelletti, D., Moroni, B., Močnik, G., Mazzola, M., Lupi, A., Becagli, S., Traversi, R., Cataldi, M., et al.: Aerosol optical properties in the Arctic: The role of aerosol chemistry and dust composition in a closure experiment between Lidar and tethered balloon vertical profiles, Science of the total environment, 686, 452–467, https://doi.org/10.1016/j.scitotenv.2019.05.399, 2019.

Filonchyk, M. and Hurynovich, V.: Validation of MODIS aerosol products with AERONET measurements of different land cover types in areas over Eastern Europe and China, Journal of Geovisualization and Spatial Analysis, 4, 1–11, https://doi.org/10.1007/s41651-020-00052-9, 2020.

Floutsi, A. A., Baars, H., Engelmann, R., Althausen, D., Ansmann, A., Bohlmann, S., Heese, B., Hofer, J., Kanitz, T., Haarig, M., Ohneiser, K., Radenz, M., Seifert, P., Skupin, A., Yin, Z., Abdullaev, S. F., Komppula, M., Filioglou, M., Giannakaki, E., Stachlewska, I. S., Janicka, L., Bortoli, D., Marinou, E., Amiridis, V., Gialitaki, A., Mamouri, R.-E., Barja, B., and Wandinger, U.: DeLiAn – a growing collection of depolarization ratio, lidar ratio and Ångström exponent for different aerosol types and mixtures from ground-based lidar observations, Atmospheric Measurement Techniques Discussions, 2022, 1–39, https://doi.org/10.5194/amt-2022-306, 2022.

Fountoukis, C. and Nenes, A.: ISORROPIA II: a computationally efficient thermodynamic equilibrium model for K^+–Ca^{2+}–Mg^{2+}–NH_4^+–Na^+–SO_4^{2-}–NO_3^-–Cl^-–H_2O aerosols, Atmospheric Chemistry and Physics, 7, 4639–4659, https://doi.org/10.5194/acp-7-4639-2007, 2007.

Freudenthaler, V.: About the effects of polarising optics on lidar signals and the $\Delta90$ calibration, Atmospheric Measurement Techniques, 9, 4181–4255, https://doi.org/10.5194/amt-9-4181-2016, 2016.

Ginoux, P., Prospero, J. M., Gill, T. E., Hsu, N. C., and Zhao, M.: Global-scale attribution of anthropogenic and natural dust sources and their emission rates based on MODIS Deep Blue aerosol products, Reviews of Geophysics, 50, https://doi.org/10.1029/2012RG000388, 2012.

Groß, S., Esselborn, M., Weinzierl, B., Wirth, M., Fix, A., and Petzold, A.: Aerosol classification by airborne high spectral resolution lidar observations, Atmospheric Chemistry and Physics, 13, 2487–2505, https://doi.org/10.5194/acp-13-2487-2013, 2013.

Groß, S., Freudenthaler, V., Schepanski, K., Toledano, C., Schäfler, A., Ansmann, A., and Weinzierl, B.: Optical properties of long-range transported Saharan dust over Barbados as measured by dual-wavelength depolarization Raman lidar measurements, Atmospheric Chemistry and Physics, 15, 11 067–11 080, https://doi.org/10.5194/acp-15-11067-2015, 2015.

Grythe, H., Ström, J., Krejci, R., Quinn, P., and Stohl, A.: A review of sea-spray aerosol source functions using a large global set of sea salt aerosol concentration measurements, Atmospheric Chemistry and Physics, 14, 1277–1297, https://doi.org/10.1016/j.atmosres.2012.09.021, 2014.

Guimarães, P., Ye, J., Batista, C., Barbosa, R., Ribeiro, I., Medeiros, A., Souza, R., and Martin, S. T.: Vertical Profiles of Ozone Concentration Collected by an Unmanned Aerial Vehicle and the Mixing of the Nighttime Boundary Layer over an Amazonian Urban Area, Atmosphere, 10, https://doi.org/10.3390/atmos10100599, 2019.

Hamilton, F. W., Gregson, F. K., Arnold, D. T., Sheikh, S., Ward, K., Brown, J., Moran, E., White, C., Morley, A. J., Bzdek, B. R., et al.: Aerosol emission from the respiratory tract: an analysis of aerosol generation from oxygen delivery systems, Thorax, 77, 276–282, https://doi.org/10.1136/thoraxjnl-2021-217577, 2022.

Hofer, J., Ansmann, A., Althausen, D., Engelmann, R., Baars, H., Fomba, K. W., Wandinger, U., Abdullaev, S. F., and Makhmudov, A. N.: Optical properties of Central Asian aerosol relevant for spaceborne lidar applications and aerosol typing at 355 and 532 nm, Atmospheric Chemistry and Physics, 20, 9265–9280, 2020.

Holben, B., Eck, T., Slutsker, I., Tanré, D., Buis, J., Setzer, A., Vermote, E., Reagan, J., Kaufman, Y., Nakajima, T., Lavenu, F., Jankowiak, I., and Smirnov, A.: AERONET—A Federated Instrument Network and Data Archive for Aerosol Characterization, Remote Sensing of Environment, 66, 1–16, https://doi.org/10.1016/S0034-4257(98)00031-5, 1998.

Hu, Q., Goloub, P., Veselovskii, I., and Podvin, T.: The characterization of long-range transported North American biomass burning plumes: what can a multi-wavelength Mie–Raman-polarization-fluorescence lidar provide?, Atmospheric Chemistry and Physics, 22, 5399–5414, https://doi.org/10.5194/acp-22-5399-2022, 2022.

Huang, W., Saathoff, H., Shen, X., Ramisetty, R., Leisner, T., and Mohr, C.: Seasonal characteristics of organic aerosol chemical composition and volatility in Stuttgart, Germany, Atmospheric Chemistry and Physics, 19, 11 687–11 700, https://doi.org/10.5194/acp-19-11687-2019, 2019.

Huesca, M., Litago, J., Palacios-Orueta, A., Montes, F., Sebastián-López, A., and Escribano, P.: Assessment of forest fire seasonality using MODIS fire potential: A time series approach, Agricultural and Forest Meteorology, 149, 1946–1955, https://doi.org/10.1016/j.agrformet.2009.06.022, special Section on Water and Carbon Dynamics in Selected Ecosystems in China, 2009.

Jiang, F., Song, J., Bauer, J., Gao, L., Vallon, M., Gebhardt, R., Leisner, T., Norra, S., and Saathoff, H.: Chromophores and chemical composition of brown carbon characterized at an urban kerbside by excitation–emission spectroscopy and mass spectrometry, Atmospheric Chemistry and Physics, 22, 14 971–14 986, https://doi.org/10.5194/acp-22-14971-2022, 2022.

Kaufman, Y., Koren, I., Remer, L., Tanré, D., Ginoux, P., and Fan, S.: Dust transport and deposition observed from the Terra-Moderate Resolution Imaging Spectroradiometer (MODIS) spacecraft over the Atlantic Ocean, Journal of Geophysical Research: Atmospheres, 110, https://doi.org/10.1029/2003JD004436, 2005.

Ke, J., Sun, Y., Dong, C., Zhang, X., Wang, Z., Lyu, L., Zhu, W., Ansmann, A., Su, L., Bu, L., et al.: Development of China's first space-borne aerosol-cloud high-spectral-resolution lidar: retrieval algorithm and airborne demonstration, PhotoniX, 3, 17, https://doi.org/10.1186/s43074-022-00063-3, 2022.

Khlebtsov, N. G., Melnikov, A. G., Bogatyrev, V. A., Dykman, L. A., Alekseeva, A. V., Trachuk, L. A., and Khlebtsov, B. N.: Can the Light Scattering Depolarization Ratio of Small Particles Be Greater Than 1/3?, The Journal of Physical Chemistry B, 109, 13 578–13 584, https://doi.org/10.1021/jp0521095, publisher: American Chemical Society, 2005.

Klett, J. D.: Lidar inversion with variable backscatter/extinction ratios, Appl. Opt., 24, 1638–1643, https://doi.org/10.1364/AO.24.001638, 1985a.

Klett, J. D.: Lidar inversion with variable backscatter/extinction ratios, Appl. Opt, 24, 1638–1643, 1985b.

Kotthaus, S., Bravo-Aranda, J. A., Collaud Coen, M., Guerrero-Rascado, J. L., Costa, M. J., Cimini, D., O'Connor, E. J., Hervo, M., Alados-Arboledas, L., Jiménez-Portaz, M., Mona, L., Ruffieux, D., Illingworth, A., and Haeffelin, M.: Atmospheric boundary layer height from ground-based remote sensing: a review of capabilities and limitations, Atmospheric Measurement Techniques, 16, 433–479, https://doi.org/10.5194/amt-16-433-2023, 2023.

Leinonen, J.: Python code for calculating Mie scattering from single- and dual-layered spheres, https://github.com/jleinonen/pymiecoated/., 2016.

Lesins, G., Chylek, P., and Lohmann, U.: A study of internal and external mixing scenarios and its effect on aerosol optical properties and direct radiative forcing, Journal of Geophysical Research: Atmospheres, 107, AAC–5, 2002.

Li, H., Liu, B., Ma, X., Jin, S., Ma, Y., Zhao, Y., and Gong, W.: Evaluation of retrieval methods for planetary boundary layer height based on radiosonde data, Atmospheric Measurement Techniques, 14, 5977–5986, https://doi.org/10.5194/amt-14-5977-2021, 2021.

Li, Z., Guo, J., Ding, A., Liao, H., Liu, J., Sun, Y., Wang, T., Xue, H., Zhang, H., and Zhu, B.: Aerosol and boundary-layer interactions and impact on air quality, National Science Review, 4, 810–833, https://doi.org/10.1093/nsr/nwx117, 2017.

Liu, C., Huang, J., Wang, Y., Tao, X., Hu, C., Deng, L., Xu, J., Xiao, H.-W., Luo, L., Xiao, H.-Y., et al.: Vertical distribution of PM2. 5 and interactions with the atmospheric boundary layer during the development stage of a heavy haze pollution event, Science of the Total Environment, 704, 135 329, https://doi.org/10.1016/j.scitotenv.2019.135329, 2020.

Liu, C., Huang, J., Tao, X., Deng, L., Fang, X., Liu, Y., Luo, L., Zhang, Z., Xiao, H.-W., and Xiao, H.-Y.: An observational study of the boundary-layer entrainment and impact of aerosol radiative effect under aerosol-polluted conditions, Atmospheric Research, 250, 105 348, https://doi.org/https://doi.org/10.1016/j.atmosres.2020.105348, 2021.

580 Liu, Z., Matsui, I., and Sugimoto, N.: High-spectral-resolution lidar using an iodine absorption filter for atmospheric measurements, Optical Engineering, 38, 1661–1670, https://doi.org/10.1117/1.602218, 1999.

Lolli, S., D'Adderio, L. P., Campbell, J. R., Sicard, M., Welton, E. J., Binci, A., Rea, A., Tokay, A., Comerón, A., Barragan, R., Baldasano, J. M., Gonzalez, S., Bech, J., Afflitto, N., Lewis, J. R., and Madonna, F.: Vertically Resolved Precipitation Intensity Retrieved through a Synergy between the Ground-Based NASA MPLNET Lidar Network Measurements, Surface Disdrometer Datasets and an Analytical

585 Model Solution, Remote Sensing, 10, https://doi.org/10.3390/rs10071102, 2018.

Marinou, E., Amiridis, V., Binietoglou, I., Tsikerdekis, A., Solomos, S., Proestakis, E., Konsta, D., Papagiannopoulos, N., Tsekeri, A., Vlastou, G., Zanis, P., Balis, D., Wandinger, U., and Ansmann, A.: Three-dimensional evolution of Saharan dust transport towards Europe based on a 9-year EARLINET-optimized CALIPSO dataset, Atmospheric Chemistry and Physics, 17, 5893–5919, https://doi.org/10.5194/acp-17-5893-2017, 2017.

590 Matthais, V., Freudenthaler, V., Amodeo, A., Balin, I., Balis, D., Bösenberg, J., Chaikovsky, A., Chourdakis, G., Comeron, A., Delaval, A., et al.: Aerosol lidar intercomparison in the framework of the EARLINET project. 1. Instruments, Applied Optics, 43, 961–976, 2004.

Matthias, V. and Bösenberg, J.: Aerosol climatology for the planetary boundary layer derived from regular lidar measurements, Atmospheric Research, 63, 221–245, 2002.

Mielonen, T., Arola, A., Komppula, M., Kukkonen, J., Koskinen, J., De Leeuw, G., and Lehtinen, K.: Comparison of

595 CALIOP level 2 aerosol subtypes to aerosol types derived from AERONET inversion data, Geophysical Research Letters, 36, https://doi.org/10.1029/2009GL039609, 2009.

More, S., Kumar, P. P., Gupta, P., Devara, P., and Aher, G.: Comparison of Aerosol Products Retrieved from AERONET, MICROTOPS and MODIS over a Tropical Urban City, Pune, India, Aerosol and Air Quality Research, 13, 107–121, https://doi.org/10.4209/aaqr.2012.04.0102, 2013.

600 Moroz, A.: Depolarization field of spheroidal particles, JOSA B, 26, 517–527, https://doi.org/10.1364/JOSAB.26.000517, publisher: Optica Publishing Group, 2009.

Munchak, L. A., Levy, R. C., Mattoo, S., Remer, L. A., Holben, B. N., Schafer, J. S., Hostetler, C. A., and Ferrare, R. A.: MODIS 3 km aerosol product: applications over land in an urban/suburban region, Atmospheric Measurement Techniques, 6, 1747–1759, https://doi.org/10.5194/amt-6-1747-2013, 2013.

605 Mylonaki, M., Giannakaki, E., Papayannis, A., Papanikolaou, C.-A., Komppula, M., Nicolae, D., Papagiannopoulos, N., Amodeo, A., Baars, H., and Soupiona, O.: Aerosol type classification analysis using EARLINET multiwavelength and depolarization lidar observations, Atmospheric Chemistry and Physics, 21, 2211–2227, https://doi.org/10.5194/acp-21-2211-2021, 2021.

Pappalardo, G., Amodeo, A., Apituley, A., Comeron, A., Freudenthaler, V., Linné, H., Ansmann, A., Bösenberg, J., D'Amico, G., Mattis, I., Mona, L., Wandinger, U., Amiridis, V., Alados-Arboledas, L., Nicolae, D., and Wiegner, M.: EARLINET: towards an advanced sustainable

610 European aerosol lidar network, Atmospheric Measurement Techniques, 7, 2389–2409, https://doi.org/10.5194/amt-7-2389-2014, 2014a.

Pappalardo, G., Amodeo, A., Apituley, A., Comeron, A., Freudenthaler, V., Linné, H., Ansmann, A., Bösenberg, J., D'Amico, G., Mattis, I., et al.: EARLINET: towards an advanced sustainable European aerosol lidar network, Atmospheric Measurement Techniques, 7, 2389–2409, 2014b.

Piironen, P. and Eloranta, E.: Demonstration of a high-spectral-resolution lidar based on an iodine absorption filter, Opt. Lett., 19, 234–236, 1994.

Poreh, M. and Cermak, J.: Study of diffusion from a line source in a turbulent boundary layer, International Journal of Heat and Mass Transfer, 7, 1083–1095, https://doi.org/10.1016/0017-9310(64)90032-8, 1964.

Prasad, A. K. and Singh, R. P.: Changes in aerosol parameters during major dust storm events (2001–2005) over the Indo-Gangetic Plains using AERONET and MODIS data, Journal of Geophysical Research: Atmospheres, 112, https://doi.org/10.1029/2006JD007778, 2007.

Qin, W., Fang, H., Wang, L., Wei, J., Zhang, M., Su, X., Bilal, M., and Liang, X.: MODIS high-resolution MAIAC aerosol product: Global validation and analysis, Atmospheric Environment, 264, 118 684, https://doi.org/10.1016/j.atmosenv.2021.118684, 2021.

Ramanathan, V., Crutzen, P. J., Kiehl, J., and Rosenfeld, D.: Aerosols, climate, and the hydrological cycle, science, 294, 2119–2124, https://doi.org/10.1126/science.1064034, 2001.

Raut, J.-C. and Chazette, P.: Vertical profiles of urban aerosol complex refractive index in the frame of ESQUIF airborne measurements, Atmospheric Chemistry and Physics, 8, 901–919, https://doi.org/10.5194/acp-8-901-2008, 2008.

Reineman, B. D., Lenain, L., and Melville, W. K.: The use of ship-launched fixed-wing UAVs for measuring the marine atmospheric boundary layer and ocean surface processes, Journal of Atmospheric and Oceanic Technology, 33, 2029–2052, https://doi.org/10.1175/JTECH-D-15-0019.1, 2016.

Romshoo, B., Müller, T., Pfeifer, S., Saturno, J., Nowak, A., Ciupek, K., Quincey, P., and Wiedensohler, A.: Optical properties of coated black carbon aggregates: numerical simulations, radiative forcing estimates, and size-resolved parameterization scheme, Atmospheric Chemistry and Physics, 21, 12 989–13 010, https://doi.org/10.5194/acp-21-12989-2021, 2021.

Rosen, J. M. and Kjome, N. T.: Backscattersonde: a new instrument for atmospheric aerosol research, Appl. Opt., 30, 1552–1561, https://doi.org/10.1364/AO.30.001552, 1991.

Salehi, M., Masoumi, A., and Moradhaseli, R.: A study on the vertical distribution of dust transported from the Tigris–Euphrates basin to the Northwest Iran Plateau based on CALIOP/CALIPSO data, Atmospheric Pollution Research, 12, 101 228, https://doi.org/10.1016/j.apr.2021.101228, 2021.

Schillinger, M., Morancais, D., Fabre, F., and Culoma, A. J.: ALADIN: the lidar instrument for the AEOLUS mission, in: Sensors, Systems, and Next-Generation Satellites VI, edited by Fujisada, H., Lurie, J. B., Aten, M. L., Weber, K., Lurie, J. B., Aten, M. L., and Weber, K., vol. 4881, pp. 40 – 51, International Society for Optics and Photonics, SPIE, https://doi.org/10.1117/12.463024, 2003.

Seidel, D. J., Ao, C. O., and Li, K.: Estimating climatological planetary boundary layer heights from radiosonde observations: Comparison of methods and uncertainty analysis, Journal of Geophysical Research: Atmospheres, 115, https://doi.org/10.1029/2009JD013680, 2010.

Smit, H. G., Straeter, W., Johnson, B. J., Oltmans, S. J., Davies, J., Tarasick, D. W., Hoegger, B., Stubi, R., Schmidlin, F. J., Northam, T., et al.: Assessment of the performance of ECC-ozonesondes under quasi-flight conditions in the environmental simulation chamber: Insights from the Juelich Ozone Sonde Intercomparison Experiment (JOSIE), Journal of Geophysical Research: Atmospheres, 112, https://doi.org/10.1029/2006JD007308, 2007.

Spiess, T., Bange, J., Buschmann, M., and Vorsmann, P.: First application of the meteorological Mini-UAV'M2AV', Meteorologische Zeitschrift, 16, 159–170, https://doi.org/10.1127/0941-2948/2007/0195, 2007.

Stocker, T.: Climate change 2013: the physical science basis: Working Group I contribution to the Fifth assessment report of the Intergovernmental Panel on Climate Change, Cambridge university press, 2014.

Tegen, I. and Schepanski, K.: Climate feedback on aerosol emission and atmospheric concentrations, Current Climate Change Reports, 4, 1–10, https://doi.org/10.1007/s40641-018-0086-1, 2018.

Tesche, M., Zieger, P., Rastak, N., Charlson, R. J., Glantz, P., Tunved, P., and Hansson, H.-C.: Reconciling aerosol light extinction measurements from spaceborne lidar observations and in situ measurements in the Arctic, Atmospheric Chemistry and Physics, 14, 7869–7882, https://doi.org/10.5194/acp-14-7869-2014, 2014.

655 Vernier, J.-P., Fairlie, T. D., Natarajan, M., Wienhold, F. G., Bian, J., Martinsson, B. G., Crumeyrolle, S., Thomason, L. W., and Bedka, K. M.: Increase in upper tropospheric and lower stratospheric aerosol levels and its potential connection with Asian pollution, Journal of Geophysical Research: Atmospheres, 120, 1608–1619, https://doi.org/10.1002/2014JD022372, 2015.

Vernier, J.-P., Fairlie, T., Deshler, T., Ratnam, M. V., Gadhavi, H., Kumar, B., Natarajan, M., Pandit, A., Raj, S. A., Kumar, A. H., et al.: BATAL: The balloon measurement campaigns of the Asian tropopause aerosol layer, Bulletin of the American Meteorological Society,
660 99, 955–973, https://doi.org/10.1175/BAMS-D-17-0014.1, 2018.

Vömel, H., David, D., and Smith, K.: Accuracy of tropospheric and stratospheric water vapor measurements by the cryogenic frost point hygrometer: Instrumental details and observations, Journal of Geophysical Research: Atmospheres, 112, https://doi.org/10.1029/2006JD007224, 2007.

Vömel, H., Naebert, T., Dirksen, R., and Sommer, M.: An update on the uncertainties of water vapor measurements using cryogenic frost
665 point hygrometers, Atmospheric Measurement Techniques, 9, 3755–3768, https://doi.org/10.5194/amt-9-3755-2016, 2016.

Wandinger, U.: Raman lidar, in: Lidar, pp. 241–271, Springer, https://doi.org/10.1007/0-387-25101-4_9, 2005.

Wandinger, U. and Ansmann, A.: Experimental determination of the lidar overlap profile with Raman lidar, Appl. Opt., 41, 511–514, https://doi.org/10.1364/AO.41.000511, 2002.

Wang, X., Bi, L., Han, W., and Zhang, X.: Single-Scattering Properties of Encapsulated Fractal Black Carbon Particles Computed Us-
670 ing the Invariant Imbedding T-Matrix Method and Deep Learning Approaches, Journal of Geophysical Research: Atmospheres, 128, e2023JD039 568, https://doi.org/10.1029/2023JD039568, _eprint: https://onlinelibrary.wiley.com/doi/pdf/10.1029/2023JD039568, 2023.

Wang, Z., Liu, C., Hu, Q., Dong, Y., Liu, H., Xing, C., and Tan, W.: Quantify the Contribution of Dust and Anthropogenic Sources to Aerosols in North China by Lidar and Validated with CALIPSO, Remote Sensing, 13, https://doi.org/10.3390/rs13091811, 2021.

Wehr, T., Kubota, T., Tzeremes, G., Wallace, K., Nakatsuka, H., Ohno, Y., Koopman, R., Rusli, S., Kikuchi, M., Eisinger, M., Tanaka, T.,
675 Taga, M., Deghaye, P., Tomita, E., and Bernaerts, D.: The EarthCARE mission – science and system overview, Atmospheric Measurement Techniques, 16, 3581–3608, https://doi.org/10.5194/amt-16-3581-2023, 2023.

Welton, E. J., Campbell, J. R., Berkoff, T. A., Valencia, S., Spinhirne, J. D., Holben, B., Tsay, S.-C., and Schmid, B.: The NASA Micro-Pulse Lidar Network (MPLNET): an overview and recent results, Opt. Pur. Apl, 39, 67–74, 2006.

Winker, D. M., Vaughan, M. A., Omar, A., Hu, Y., Powell, K. A., Liu, Z., Hunt, W. H., and Young, S. A.: Overview of the
680 CALIPSO mission and CALIOP data processing algorithms, Journal of Atmospheric and Oceanic Technology, 26, 2310–2323, https://doi.org/10.1175/2009JTECHA1281.1, 2009.

Xiafukaiti, A., Lagrosas, N., Ong, P. M., Saitoh, N., Shiina, T., and Kuze, H.: Comparison of aerosol properties derived from sampling and near-horizontal lidar measurements using mie scattering theory, Applied Optics, 59, 8014–8022, https://doi.org/10.1364/AO.398673, 2020.

685 Xiang, Y., Zhang, T., Liu, J., Lv, L., Dong, Y., and Chen, Z.: Atmosphere boundary layer height and its effect on air pollutants in Beijing during winter heavy pollution, Atmospheric Research, 215, 305–316, https://doi.org/https://doi.org/10.1016/j.atmosres.2018.09.014, 2019.

Xue, Q., Nie, W., Guo, L., Liu, Q., Hua, Y., Sun, N., Liu, C., and Niu, W.: Determining the optimal airflow rate to minimize air pollution in tunnels, Process Safety and Environmental Protection, 157, 115–130, https://doi.org/10.1016/j.psep.2021.10.039, 2022.

690 Yao, Y., Curtis, J. H., Ching, J., Zheng, Z., and Riemer, N.: Quantifying the effects of mixing state on aerosol optical properties, Atmospheric Chemistry and Physics, 22, 9265–9282, https://doi.org/10.5194/acp-22-9265-2022, 2022.

Zarco-Tejada, P., González-Dugo, V., and Berni, J.: Fluorescence, temperature and narrow-band indices acquired from a UAV platform for water stress detection using a micro-hyperspectral imager and a thermal camera, Remote Sensing of Environment, 117, 322–337, https://doi.org/https://doi.org/10.1016/j.rse.2011.10.007, remote Sensing of Urban Environments, 2012.

695 Zhang, H., Wagner, F., Saathoff, H., Vogel, H., Hoshyaripour, G., Bachmann, V., Förstner, J., and Leisner, T.: Comparison of Scanning LiDAR with Other Remote Sensing Measurements and Transport Model Predictions for a Saharan Dust Case, Remote Sensing, 14, https://doi.org/10.3390/rs14071693, 2022.

Zhang, M., Tian, P., Zeng, H., Wang, L., Liang, J., Cao, X., and Zhang, L.: A comparison of wintertime atmospheric boundary layer heights determined by tethered balloon soundings and lidar at the site of SACOL, Remote Sensing, 13, 1781, https://doi.org/10.3390/rs13091781, 700   2021.

Zhen, Z., Jiang, S., and Ma, K.: Automatic carrier landing control for unmanned aerial vehicles based on preview control and particle filtering, Aerospace Science and Technology, 81, 99–107, https://doi.org//10.1016/j.ast.2018.07.039, 2018.

Zieger, P., Weingartner, E., Henzing, J., Moerman, M., de Leeuw, G., Mikkilä, J., Ehn, M., Petäjä, T., Clémer, K., van Roozendael, M., Yilmaz, S., Frieß, U., Irie, H., Wagner, T., Shaiganfar, R., Beirle, S., Apituley, A., Wilson, K., and Baltensperger, U.: Comparison of 705   ambient aerosol extinction coefficients obtained from in-situ, MAX-DOAS and LIDAR measurements at Cabauw, Atmospheric Chemistry and Physics, 11, 2603–2624, https://doi.org/10.5194/acp-11-2603-2011, 2011.

Zieger, P., Kienast-Sjögren, E., Starace, M., von Bismarck, J., Bukowiecki, N., Baltensperger, U., Wienhold, F. G., Peter, T., Ruhtz, T., Collaud Coen, M., Vuilleumier, L., Maier, O., Emili, E., Popp, C., and Weingartner, E.: Spatial variation of aerosol optical properties around the high-alpine site Jungfraujoch (3580 m a.s.l.), Atmospheric Chemistry and Physics, 12, 7231–7249, https://doi.org/10.5194/acp-710   12-7231-2012, 2012.

Zieger, P., Aalto, P. P., Aaltonen, V., Äijälä, M., Backman, J., Hong, J., Komppula, M., Krejci, R., Laborde, M., Lampilahti, J., de Leeuw, G., Pfüller, A., Rosati, B., Tesche, M., Tunved, P., Väänänen, R., and Petäjä, T.: Low hygroscopic scattering enhancement of boreal aerosol and the implications for a columnar optical closure study, Atmospheric Chemistry and Physics, 15, 7247–7267, https://doi.org/10.5194/acp-15-7247-2015, 2015.